

THE RELATIONSHIP BETWEEN X-RAY LUMINOSITY AND MAJOR FLARE LAUNCHING IN GRS 1915+105

BRIAN PUNSLY¹ AND JÉRÔME RODRIGUEZ²

Draft version June 29, 2018

ABSTRACT

We perform the most detailed analysis to date of the X-ray state of the Galactic black hole candidate GRS 1915+105 just prior to (0 to 4 hours) and during the brief (1 to 7 hour) ejection of major (superluminal) radio flares. A very strong model independent correlation is found between the 1.2 keV - 12 keV X-ray flux 0 to 4 hours before flare ejections with the peak optically thin 2.3 GHz emission of the flares. This suggests a direct physical connection between the energy in the ejection and the luminosity of the accretion flow preceding the ejection. In order to quantify this concept, we develop techniques to estimate the intrinsic (unabsorbed) X-ray luminosity, $L_{\text{intrinsic}}$, from RXTE ASM data and to implement known methods to estimate the time averaged power required to launch the radio emitting plasmoids, Q (sometimes called jet power). We find that the distribution of intrinsic luminosity from 1.2 keV - 50 keV, $L_{\text{intrinsic}}(1.2 - 50)$, is systematically elevated just before ejections compared to arbitrary times when there are no major ejections. The estimated Q is strongly correlated with $L_{\text{intrinsic}}(1.2 - 50)$ 0 to 4 hours before the ejection, the increase in $L_{\text{intrinsic}}(1.2 - 50)$ in the hours preceding the ejection and the time averaged $L_{\text{intrinsic}}(1.2 - 50)$ during the flare rise. Furthermore, the total time averaged power during the ejection (Q + the time average of $L_{\text{intrinsic}}(1.2 - 50)$ during ejection) is strongly correlated with $L_{\text{intrinsic}}(1.2 - 50)$ just before launch with near equality if the distance to the source is ≈ 10.5 kpc.

Subject headings: Black hole physics — X-rays: binaries — accretion, accretion disks

1. INTRODUCTION

Microquasars are Galactic X-ray binaries known to be sources of relativistic jets (Mirabel et al 1992). It is now clear that microquasars exhibit at least two drastically different types of jets: discrete ejections of 'plasmoids' Mirabel and Rodriguez (1994) usually associated with transition from spectrally hard states to soft states (e.g. Fender et al (2004)), while a so-called compact jet is present during the hard state (Corbel et al (2000, 2003); Gallo et al (2003)) and is quenched at the transition to the soft state (Fender et al 1999b). If the accretion of matter by the strong gravitational field due to the presence of the black hole is natural, the ejection of particles at relativistic speeds is mysterious, and still largely unknown. Huge multi-wavelength efforts have been made in the past twenty years to try and understand the origin of all type of jets and their connection to the accretion processes (e.g. Mirabel et al (1998); Corbel et al (2000, 2003); Klein-Wolt et al (2002); Gallo et al (2003); Rodriguez et al (2008a,b); Rushton et al (2010)). The Galactic black hole candidate GRS 1915+105 is well known for launching superluminal radio flares out to large distances (Mirabel and Rodriguez 1994; Rodriguez and Mirabel 1999; Fender et al 1999a; Miller-Jones et al 2005). In fact, there is no other known Galactic black hole that has produced nearly as many strong radio flares that have been observed to be superluminal. GRS 1915+105 is known to show the two main types of jets (Mirabel and Rodriguez 1994; Dhawan et al 2000; Fuchs et al 2003). Discrete ejection, in this source, are

further separated into to superluminal ejections (resulting in major \geq a few 100 mJy radio flares), and smaller 'bubble' ejections³ showing sometimes a repetitive pattern (radio oscillations; e.g. Klein-Wolt et al (2002); Vadawale et al (2003)). The X-ray luminosity of GRS 1915+105 is also one of the highest of any known Galactic black hole candidate (Done et al 2004). The existence of both relativistic outflows and high continuum luminosity make it tempting to speculate that GRS 1915+105 might be a scaled down version of a radio loud quasar. This is of particular importance because the time scales for evolution are reduced from the AGN (active galactic nuclei) time scales of thousands to hundreds of thousands of years to orders of seconds or hours. Thus, unlike quasars, it is in principle possible to see a temporal connection between the putative accretion flow (X-ray luminosity) and the superluminal jet launching mechanism.

Studies have been performed in the case of the small bubble ejections (Fender et al 1997; Pooley and Fender 1997; Mirabel et al 1998; Klein-Wolt et al 2002; Rodriguez et al 2008a). These ejections are always preceded/occur as response to a hard X-ray dip, with a length that correlates with the radio flare amplitude, ended by a short soft X-ray spike that is the trigger of the ejection (Rodriguez et al 2008a,b; Prat et al 2010).

More to the point, there are also anecdotal coarsely time sampled discussions of the actual major flares. As

¹ 1415 Granvia Altamira, Palos Verdes Estates CA, USA 90274 and ICRA Net, Piazza della Repubblica 10 Pescara 65100, Italy, brian.punsly1@verizon.net or brian.punsly@comdev-usa.com

² Laboratoire AIM, CEA/DSM-CNRS-Université Paris Diderot, IRFU SAp, F-91191 Gif-sur-Yvette, France.

³ The discriminant between major flares and minor flares in our analysis is based on our working definition of a major flare. Major flares are defined as flares with radio spectra that evolve from being flat spectrum at 15 GHz and lower frequency to being steep spectrum at 2.3 GHz with a flux density level of at least 100 mJy (where a two point spectral index from 2.3 GHz to 8.3 GHz of 0.5 is used to divide steep from flat spectrum). Typically, if a minor flare is ever detected as steep spectrum at 2.3 GHz, the flux density is less than 10 mJy.

an extrapolation of the discussion above on X-ray cycles for optically thick flares, there is the analogy to the major flares that has been perceived in some instances. The appeal of these arguments is that it would unify all the radio behavior of GRS 1915+105. X-ray dips in hard states preceding major flares that occur on the order of days (as opposed to minutes as for the minor flares) before the major flares start were noted in (Dhawan et al 2004). There is also mention of "associated" soft X-ray spikes that appear when there are major flares (Trushkin et al 2007; Fender et al 2004; Dhawan et al 2004; Vadawale et al 2003). The time relation between the soft spike and the radio flare is, however, not as clear as for the bubble ejections. Thus, considering the rapid rise of the major flares (a few hours), we believe that a more contemporaneous analysis is required in order to make a physical connection between the X-ray emission and the major flare launching mechanism. The only way to assess this is by means of a detailed study of a large database of major flares.

Thusly motivated, this paper describes a program of study aimed at determining the X-ray connection to major flares on the relevant time scales of hours with existing long term archival data. Clearly, minute by minute or second by second X-ray and wide-band radio monitoring would tell us the answer, but it is not available and impractical to collect. So we must settle for imperfect minute to hour time resolution to get the best available insight.

The major flares in GRS 1915+105 occur at irregular intervals a few times a year. The characteristic timescales for this system can be very short, seconds to hours. Triggered observations only occur after the bulk or all of the flare launching is over (eg, Dhawan et al (2004)). Triggered radio observations of these flares with MERLIN, VLA and VLBA and X-ray observations typically take place a day or more after the ejection has occurred (Mirabel and Rodriguez 1994; Rodriguez and Mirabel 1999; Fender et al 1999a; Dhawan et al 2000). The major flares initiate unexpectedly on average a few times a year. Thus, the actual initiation is very rarely detected in the radio monitoring. Similarly, X-ray observations are only serendipitous before unpredictable flare ejections and therefore are generally too far spaced in time to be causally connected to the launch mechanism. Thus, to our knowledge, all previous accounts of X-ray connections to the major ejections have been based on time sampling that is far too coarse (\sim days) to uncover any causal relationships between the state of the X-ray emitting plasma and the powerful ejections.

Being cognizant of the discrepancy between the density of the time sampling of data acquisition around the launch time of major flares and the major flare ejection time scale, a search for major flares with high time resolution data sampling near the launch time was initiated. We have found 11 major ejection events in which we have sufficient information to assess the X-ray state before and/or during flare launch and its connection to the energy of the ejected plasmoids in major flares.

Our program has four main components, The first is finding suitable major flare epochs that can be used for analysis as described in Section 2. Secondly, we review and develop methods for estimating the energy contained within a plasmoid from the time evolution of the optically

thin low radio spectrum (Section 3). Thirdly, we determine conversion techniques in order to interpret RXTE fluxes as intrinsic X-ray luminosity (Section 4). Finding an algorithm to convert ASM fluxes to 1.2 - 50 keV intrinsic luminosity, $L_{\text{intrinsic}}(1.2 - 50)$, was the most labor intensive effort and required attention to many technical points. In the last portion of the program, we correlate the directly measured quantities as well as the model dependent intrinsic physical quantities in order to shed light on any underlying causal relationships in the flare launching mechanism (Section 5).

2. A CATALOG OF MAJOR FLARES WITH HIGH TEMPORAL RESOLUTION

Numerous studies of AGNs and GRS 1915+105 in particular have indicated that optically thin low frequency radio emission is a robust surrogate for determining the energy contained within the plasma responsible for said emission (Rawlings and Saunders 1991; Willott et al 1999; Punsly 2012). This is discussed in detail in the next section where we make our estimates of ejected plasmoid energy. In GRS 1915+105, it was demonstrated that knowledge of the peak of the optically thin flux at low frequency (2.3 GHz in this case) and the spectral index at late times in the flare evolution removes many unknown variables from the energy estimate when the data it is considered in the context of an evolving plasmoid (Punsly 2012). The requirement of sufficient data to implement this method greatly restricts the available data set for our work. We find that only the GBI (Green Bank Interferometer) survey has sufficient low frequency data time sampling density at 2.3 GHz to define the peak of the optically thin flux from an episodic ejection and show its late time behavior (The GBI data was downloaded from the public access web sites: <ftp://ftp.gb.nrao.edu/pub/fghigo/gbidata/gdata/1915+105> and the older data which was referenced but did not survive the culling process that is defined below <http://www.gb.nrao.edu/fgdocs/gbi/arcgbi/1915+105>). The GBI monitoring ended in 2000. This motivated the following order of culling criteria

1. A flare was loosely defined as 70 mJy of optically thin flux at 2.3 GHz, keeping in mind that the gaps in temporal coverage might miss the true peak (which could very well be somewhat larger, \sim 100 mJy). The optically thin condition is defined by a spectral index, $\alpha > 0.5$ based on the convention that the flux density follows a power law in frequency, $S_{\nu} \sim \nu^{-\alpha}$. An estimate of the peak optically thin radio flux at 2.3 GHz allows us to estimate the energy stored in the plasmoid. We use GBI monitoring data to minimize temporal gaps in the coverage.
2. The next step was to use the 8.3 GHz flux density from the GBI survey and 15 GHz flux density from the Ryle Telescope monitoring program (see the public archive <http://www.mrao.cam.ac.uk/guy/1915/> that has been generously provided by Guy Pooley) to find epochs in which the initial period of optically thick emission that precedes a corresponding optically thin peak at 2.3 GHz had sufficient high frequency

TABLE 1
MAJOR FLARES ^a

Estimated Flare Start (MJD)	RXTE Date ^b (MJD)	Δ (hours)	End of Ejection (MJD)	Estimated Flux Density 2.3 GHz at $\tau = 0.1$ (mJy)	Observed Peak Optically Thin 2.3 GHz Flux Density (mJy)	Type based on Figure 12	α ^c	Light Curve Extrapolation Time ^d (hrs)
50590.160	50590.157 (ASM)	0.05	50590.200	74 ± 13	63 ± 6	1	0.57	0
50750.520 ± 0.02	50750.351 (ASM)	4.53	50750.695 ± 0.055	490 ± 58	548 ± 55	2 or 3	0.57	0.74-1.68
50916.140 ± 0.04	50916.089/50916.146 (ASM) ^e	0.82	50916.49	702 ± 129	592 ± 59	1	0.52	4.80 - 6.72
50967.200	50967.148 (ASM)	1.26	50967.33	516 ± 180	343 ± 34	1	0.67	0
51003.070	51002.907 (ASM)	3.91	51003.20 ± 0.02	234 ± 29	251 ± 25	2	0.81	0
51270.330	51270.315 (ASM)	0.36	51270.45 ± 0.04	146 ± 21	145 ± 15	2 or 3	0.54	0.57
51336.970	51336.940 (ASM)	0.72	51337.18 ± 0.06	470 ± 49	484 ± 48	2 or 3	0.70	0
51375.150	51375.099 (ASM)	1.22	51375.28	196 ± 25	180 ± 18	1	0.60	0
51499.702	51499.614 (ASM)	2.11	51499.875	399 ± 115	358 ± 36	1	0.76	2.04
51535.630	51535.556 (ASM)	1.77	51535.83	512 ± 114	512 ± 51	1, 2 or 3	0.23 ^f	0.93
51602.506	51602.361 (PCA)	3.48	51602.63	125 ± 13	115 ± 12	1 or 3	0.80	0

^aCatalogue of the major flares compliant to our observational requirements (see text).

^bThe closest (in time) RXTE X-ray observation date that preceded the estimated flare ejection time. All data is with the ASM except for the last entry which is with the PCA.

^cThe spectral index when the peak optically thin 2.3 GHz flux density was measured.

^dLength of time in hours of the gap in coverage between radio data and the estimated start of the flare.

^eDepending on the exact flare initiation time, the observation 50916.089 or 50916.146 could be the closest RXTE observation that precedes the flare

^fTechnically not optically thin, but see the caption of Figure 10 for an explanation of the inclusion in the sample

coverage to estimate the beginning of the rise in optically thick flux.

- We then applied a further constraint from the 8.3 GHz GBI data and the 15 GHz Ryle data that the peak of the optically thick emission was either observed or fell within an observing gap less than \sim an hour wide. Steps 2 and 3 provide a rise time estimate and by 1), above, also an estimate of the time averaged power required to eject the plasmoids.
- The last step was the most critical. We looked through the RXTE ASM and PCA (Proportional Counter Array) archives to find any of the epochs that passed the first three steps of the culling process that also had an X-ray observation to within 4 hours of the initiation of a major ejection. In practice, RXTE pointing observations that allow the exploitation of the PCA capabilities (wide-band and large number statistics) rarely fall serendipitously just before a major ejection. Thus, for the most part, the epochs considered here have the more narrow range of coverage provided by the three spectral band measurements of the ASM.

The light curves in Figures 1 - 11, allow us to see the estimates of the flare initiation time, the end of the flare ejection, and the peak optically thin flux juxtaposed to the dates of X-ray data capture. The horizontal and vertical scales on the axes are optimized for estimates of flare rise times and locating the peak optically thin flux density. In the light curves, one can see that the slowly evolving peak in optically thin emission often clearly lies within gaps in the GBI coverage. This leads to an uncertainty in the peak optically thin flux. The value in column (5) is the largest possible spread in the peak value that is consistent with the observations. This is critical to our calculations as the models of the December 1993 flares indicate that this flux maximum occurs near the time that the plasmoid has an optical depth $\tau \approx 0.1$. As

such, we use this flux density level (with its considerable uncertainty) as a surrogate for knowing the flux density when $\tau \approx 0.1$. The extremes of this spread in possible flux density when $\tau = 0.1$ are indicated by the black arrows in the light curves in Figures 1 - 11. The error in column (5) represents the largest deviation from the average of this spread. By contrast, column (6) is the largest optically thin 2.3 GHz flux density taken directly from the measurements. The latter idea is probably less accurate because it does not compensate for the large gaps in observing coverage that are likely to miss the exact peak. This cut the total number of major flares to just 11. Thus, only the strongest correlations would be statistically significant from such a small sample.

2.1. Determining the Start of the Flare

Knowledge of the start of the flare is essential for our analysis. It allows us to establish a temporal (and perhaps causal) chain of events. It is this information that provides the key time signature for the precise physical significance of individual X-ray observations. Every optically thin flare is preceded by a rise in optically thick high frequency radio emission. As the ejected plasmoid expands, the optical depth to synchrotron self absorption (SSA) decreases and the spectrum steepens at ever decreasing frequency until it is optically thin at our frequency of observation, 2.3 GHz. The highest frequency observations that we have in general are the 15 GHz Ryle telescope data and 8.3 GHz GBI data. We consider a rise in these data as an indication of a flare initiation if it extrapolates in time to increased flux and optically thin 2.3 GHz emission. ⁴

In order to define the initiation of the flare, we need to extrapolate the 15 GHz or 8.3 GHz light curve back-

⁴ The optically thin nature is critical since GRS 1915+105 can have extraordinarily strong optically thick compact jets (\sim hundreds of mJy), the so-called "high plateau" state (Fuchs et al 2003).

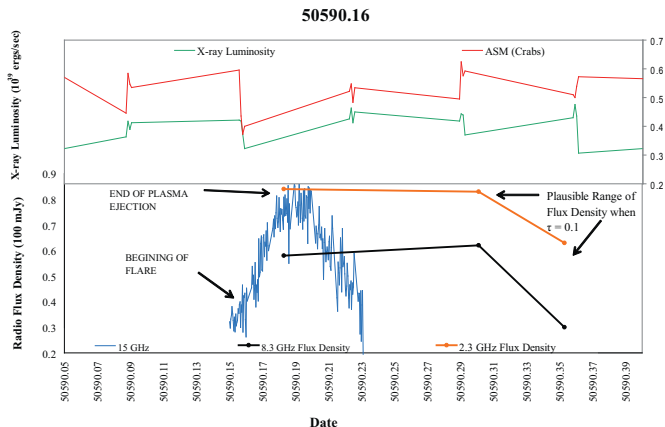


FIG. 1.— The top frame shows the X-ray light curves for the flare that was initiated at approximately MJD 50590.16, the ASM flux in Crabs and the intrinsic unabsorbed X-ray luminosity estimated from the analysis in Section 4 (an assumed distance of 11 kpc is used throughout the paper unless otherwise stated) in units of 10^{39} ergs/s. The radio data is plotted in the bottom frame in units of 100 mJy. The 2.3 GHz coverage has gaps in it. A range of plausible values for the flux density when the synchrotron self absorption SSA optical depth = 0.1 are indicated by black arrows. The method of designating this feature and the format of the split frame figure are common to all the light curves presented in Figures 1 - 11. This is a weak flare by the standards of this paper and might be a very strong version of a “bubble” flare or “baby jet.” Thus, it represents an important member of the sample because it bridges the gap in power between the two classes of discrete ejections that are discussed in the Introduction. Formally X-ray observations precede the flare start time, but some X-ray observations exist within a range spanned by the 10% uncertainty the was assigned to all flare start time estimates in Section 2.1.

wards in time a few minutes to a few hours (i.e., there is not complete temporal coverage). There are two considerations here that are required for the sake of accuracy. First of all, we only select flares where the light curve produces very short extrapolations in time, typically less than one hour (see column 9 of Table 1). Exceptions are only made for some of the extremely strong flares that are desirable to study for their strength and for making connections to previous published studies of these conspicuous flares. Even so, the average extrapolation in Table 1 is less than one hour. Secondly in order to execute this criteria, one must define when the emission has actually begun to rise above the background flux. We can establish the background flux by the level of the flux in the previously measured epoch. So an additional requirement for an epoch to have an acceptable data set is having other measurements close enough in time (less than one day) before the flare so that a background flux level can be estimated at 8.3 GHz or 15 GHz. When the extrapolated flux density level intersects the background level, this is considered the start of the flare. The background levels are usually between 10 mJy - 30 mJy for the 15 GHz light curves and 20 - 40 mJy for the 8.3 GHz light curves. Because the levels are so low and the rise is so steep this leads to minimal errors in the estimations of the beginning of the flare rise. In order to deal with this uncertainty, we liberally assign a 10% error to all our flare initiation time estimates and all our flare end time estimates in the final calculation of ejection power. Additional uncertainties in the flare initiation time due to

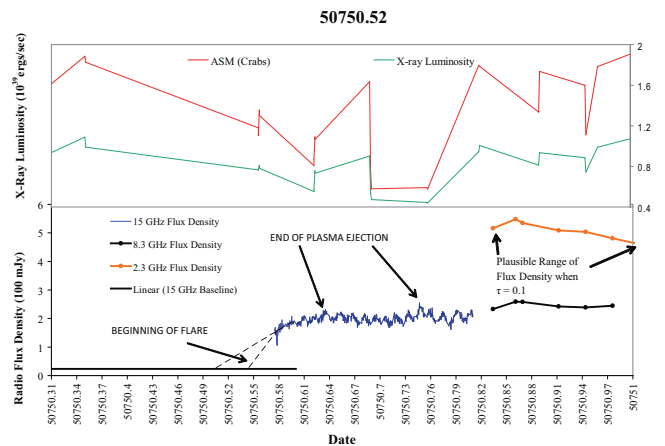


FIG. 2.— We perform two estimates of the flare initiation time that are represented by the two dashed straight black lines that extend from the 15 GHz light curve to the 15 GHz background flux density level. There is significant curvature in the light curve which leads to uncertainty in the extrapolation. The steeper extrapolation is based on the linear least squares fit to the first 10 minutes of 15 GHz data and the other extrapolation is based on the fit to the first 30 minutes. This yields an estimated initiation date MJD 50750.50 ± 0.04 for this flare. After the first local maximum in the 15 GHz light curve at 50750.64, there is a slight rate of increase, peaking again at 50750.74. Superimposed on this are what appear to be strong core oscillations. Thus, the true endpoint of the injection is obscured leading to significant uncertainty. We carry the range of uncertainty in both the initiation and end of the episode of plasma ejection throughout our calculations.

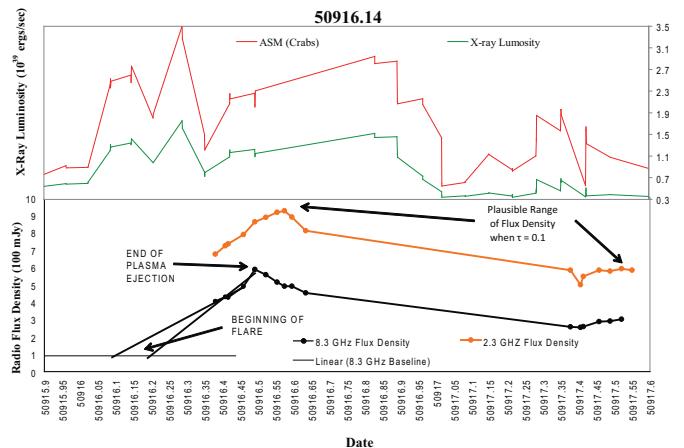


FIG. 3.— The flare that was initiated at approximately MJD 50916.14 ± 0.04 is the most luminous at 2.3 GHz of any flare in the sample. The extrapolation from the 8.3 GHz light curve to the flare initiation time is the longest in the sample. Due to the sparse data and the large extrapolation (\sim hours), we consider two extrapolations, one based on the first three points of the 8.3 GHz light curve and the other based on all 4 points that comprise the rise in the flux density. The extrapolations are represented by the straight black lines. This results in uncertainty in the estimation of the flare start time that manifests itself as a source of uncertainty in our calculations of the power required to eject the plasma. The abrupt change in the 8.3 GHz light curve from an increase to a decrease seems to be a clear signal of the end of the energy injection as opposed to adiabatic cooling.

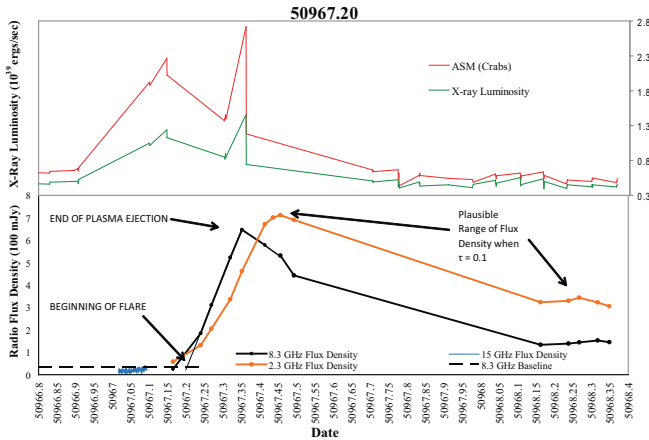


FIG. 4.— The flare that was initiated at approximately on MJD 50967.20 is very strong with a very abrupt rise. There is a large uncertainty in the peak optically thin flux density at 2.3 GHz due to an inopportune gap in the GBI coverage. This creates a large source of error in our energy estimates. The rise in the 8.3 GHz light curve is very linear and its extrapolation (the straight black line) appears to dive into a background level of random fluctuations (crosses the dashed 8.3 GHz baseline flux density). The 8.3 GHz light curve changes from a uniform linear increase to a decrease very abruptly which seems to represent the ejection mechanism turning off as opposed to gradual, continuous ageing or cooling effects.

the details of the light curve data sampling are described in detail and are quantified numerically and carried as an additional source of error in all calculations.

It is important to justify the definition of the beginning of the flare. Consider an optically thick source with an expanding radius, $r = f(t)r_0$, where r_0 is a constant and $f(t)$ is a scale factor which for uniform expansion is proportional to elapsed time. If the source is observed well below the SSA cutoff frequency, Moffet (1975) showed that the spectral luminosity will scale in time as

$$L_\nu(t) \sim f^3, \text{ for uniform expansion } L_\nu(t) \sim t^3. \quad (1)$$

Equation (1) is true for all frequencies well below the SSA cutoff frequency. Thus, the luminosity will begin to increase at all frequencies that are well below cutoff, simultaneously. However the rate of increase will be less for lower frequencies due to the increased SSA opacity which scales like $\nu^{-(2.5+\alpha)}$, where α is the spectral index (Moffet 1975). Thus, all light curves that are based on optically thick fluxes at a single frequency during the entire flare rise should extrapolate back to the same flare initiation time. One cannot combine fluxes at different frequencies in the same light curve extrapolation. The higher the frequency, the quicker that the flux density rises to levels above the background noise level making the early stages of flare rise more discernible than at lower frequency. This raises the question if using 8.3 GHz as opposed to 15 GHz will make a significant difference to the estimate of the flare start. Using the light curves in Figures 4, 5, 10 and 11 allows us to assess this by estimating flare start times with both 8.3 GHz and 15 GHz (per the methods described in this section). For the 8.3 GHz estimate we have a -0.02 day (lead) to 0.03 day (lag) offset for epoch MJD 51536.63, 0.00 to $+0.03$ days

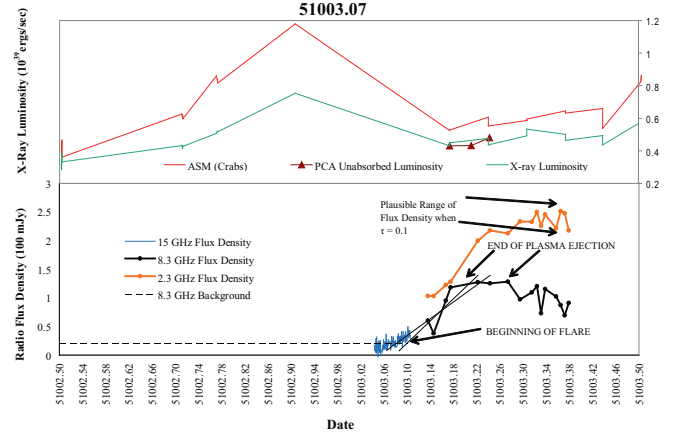


FIG. 5.— The flare that was initiated at approximately MJD 51003.07 has both ASM and PCA X-ray data in the top frame. The PCA data (discussed in section 4.4.2) was taken at what we estimate to be the last few minutes to an hour of the plasma injection. Notice how accurately the luminosity based on our narrow band ASM estimator at this same time agrees with the broad band intrinsic X-ray luminosity based on the detailed models of the PCA data. The slow turnover following the abrupt rise makes the interpretation of the end of the rise in the light curve ambiguous and introduces some error. The rapid increase in the two point spectral index from 2.3 GHz to 8.3 GHz after the terminus of the steep rise of the 8.3 GHz light curve is evidence of large optical depth changes due to adiabatic expansion. The extrapolation of the 8.3 GHz light curve to the background level (dashed black line) from 14 hours earlier has some uncertainty due to large fluctuations during the rise. Two representative fits (one a linear least squares fit to the first 5 points and one based on the first 6 points of the light curve) that are consistent with the estimated flare end time are plotted as black straight lines. The 15 GHz data has denser data sampling that seems to straddle the flare initiation time and clearly provides a better estimate of the start time.

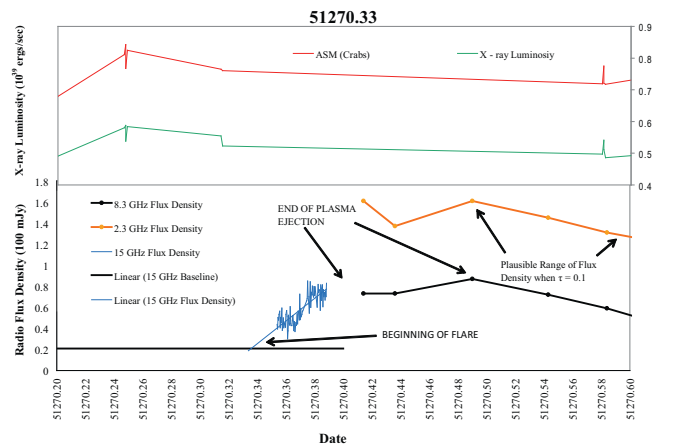


FIG. 6.— The flare that initiated on approximately MJD 51270.33 has a gap in the data coverage near the peak of the flare rise at 15 GHz. The coverage resumes at 8.3 GHz which leaves a large uncertainty in the estimate of the end of the plasma ejection episode.

offset for epoch MJD 51003.07, < 0.12 days offset for MJD 50967.20 and < 0.15 days offset for MJD 51602.51 (hereafter we will drop the MJD from the dates for the sake of brevity). The upper limits represent the gap in the data sampling, not a perceivable difference in flare initiation estimates. This small uncertainty seems to be

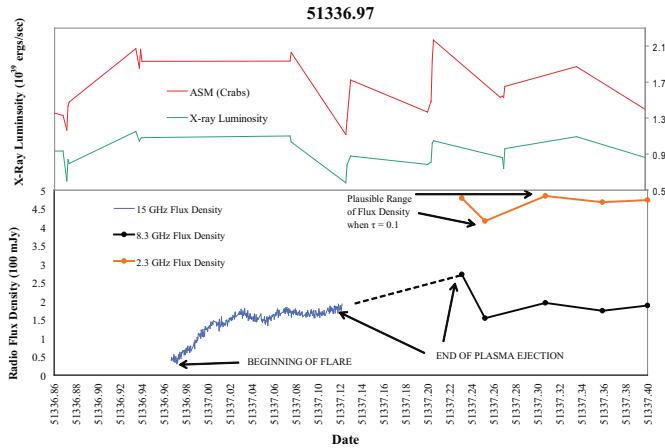


FIG. 7.— The flare that was initiated at approximately MJD 51336.97 has excellent data sampling at 15 GHz during flare initiation. The flare end time has some major uncertainty because of strong oscillations superimposed on a slow rise in the light curve from 51337.03 to 51337.13. Then there is a gap of 0.1 days until coverage is resumed at 8.3 GHz which adds even more uncertainty. The abrupt change in the 8.3 GHz light curve after 51337.231 seems to indicate a distinct change in the plasma dynamics and the latest possible estimate for the end of the flare. This flare and the VLBA observations are discussed in detail in Section 2.2.

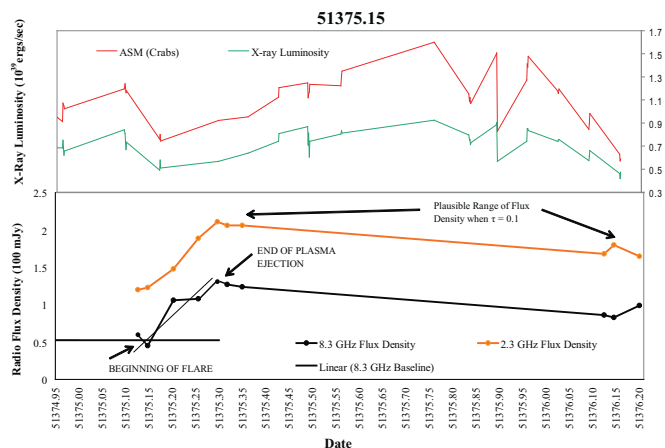


FIG. 8.— The flare that was initiated at approximately MJD 51375.15 has complete 8.3 GHz coverage of the flare rise. However, there is a large gap in the observation following this. There is fortuitous ASM data (top frame) before and during the flare rise. This is a modest flare that emerges from one of the highest background flux levels of any flare. This combination of circumstances manifests itself as a large uncertainty in the spectral index of the optically thin emission in Table 2, columns 2 and 3.

accommodated by our choice of 10% error on all flare initiation and end time estimates (that was noted above).

Due to the short duration of the light curve extrapolations in Table 1 and the frequency independent implications of Equation (1), we conclude that light curve extrapolation is a robust method of estimation that should be more accurate than extrapolating ballistic motion from long baseline radio interferometry 53 to 77 hours after initiation as in Fender et al (1999a). One reason for adding the flare from epoch 50750.50 to the sample in spite of the relatively long light curve extrapolation times of 0.74 - 1.68 hours is the fact that this is a well

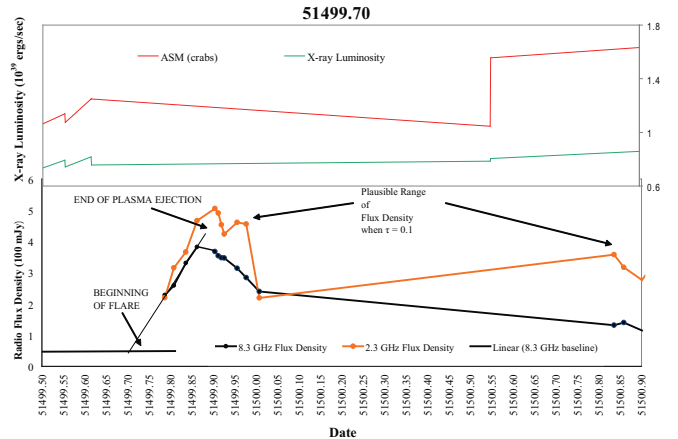


FIG. 9.— The strong flare that was initiated at approximately MJD 51499.70 has good coverage all the way to the end of the nearly linear steep rise of the 8.3 GHz light curve. The 2.3 GHz flux density drops abruptly near 51500.00. This type of drastic dip is not seen in any other of the 2.3 GHz light curves. This "out of family" behavior likely indicates a problem with the observation or the data reduction.

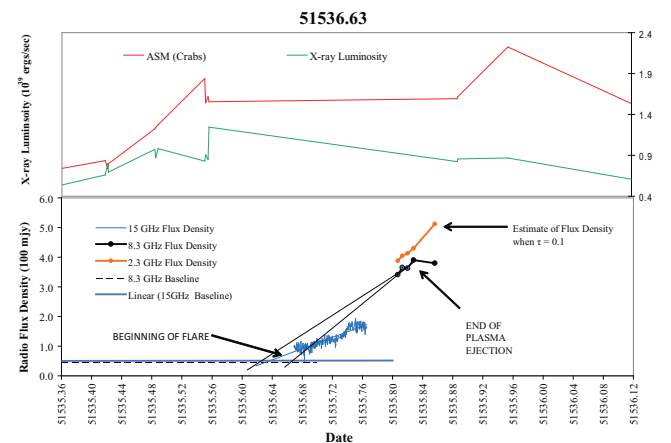


FIG. 10.— The strong flare initiated on MJD 51535.63 was included in the sample even though $\alpha < 0.5$. Unfortunately, the peak in the optically thin flux at 2.3 GHz was most likely missed by a large gap in GBI coverage. The light curve had clearly peaked at 8.3 GHz and was in the process of evolving towards being optically thin between 2.3 GHz and 8.3 GHz when the data collection stopped. We also have a good estimate of the flare start time from the 15 GHz light curve and ASM data just before this. Since the flare was very strong and the rise time could be estimated accurately, we included it in the sample and just carried a large error in the peak optically thin flux at 2.3 GHz. Due to the sparse data at 8.3 GHz and the large extrapolation (\sim hours) to the flare start time, we consider two linear extrapolations, one based on the first three points of the 8.3 GHz light curve and the other based on all 4 points that comprise the rise in the flux density. The extrapolations are represented by the straight black lines. The 15 GHz data has denser data sampling and requires a shorter extrapolation to the initiation time and therefore provides a better estimate of the start time.

studied flare, (Fender et al 1999a; Dhawan et al 2000), and it is very strong. We can check the validity of our assumptions and method by comparing the estimated initiation times. Using MERLIN observations 53 to 77 hours later Fender et al (1999a) estimate an initiation date of

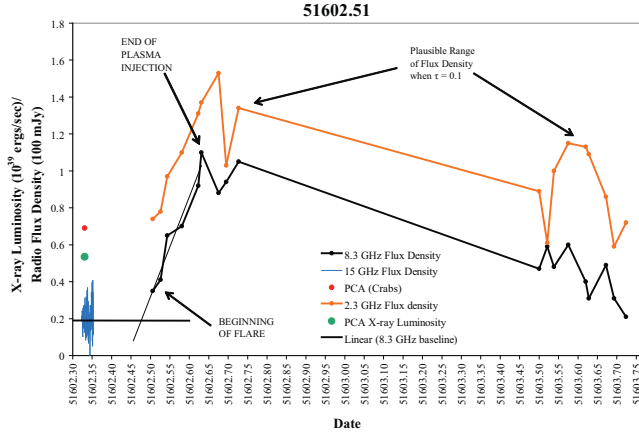


FIG. 11.— The light curves for the flare that was initiated at approximately MJD 51602.506. This is the only epoch with PCA observations immediately preceding the flare onset.

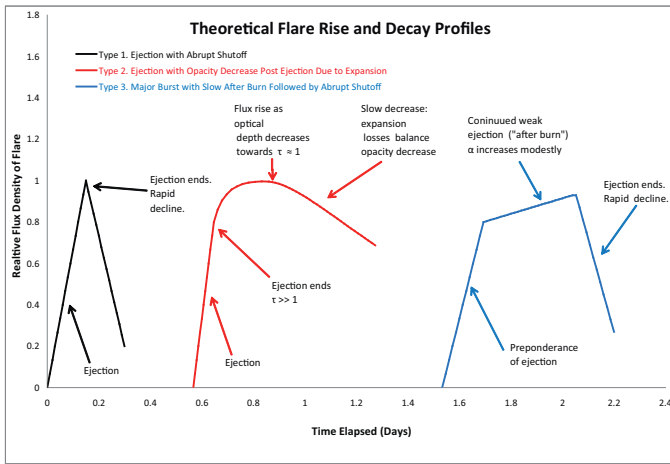


FIG. 12.— Generic light curves based on different theoretical assumptions. See the text of Section 2.2 for details.

50749.8 to 50750.08, we estimate 50750.00 to 50750.04. The agreement in the two methods and the fact that the light curve extrapolation has less uncertainty is corroboration of the discussion of the robustness of this method that was given above. We expect estimates with shorter extrapolations to be equally or more accurate.

2.2. Determining the End of the Plasma Ejection Episode

Knowing both the beginning and the end of the ejection episode is a valuable piece of information as it allows for a conversion of the energy in the ejection to the time averaged power required to eject the plasmoid. Since the existence of an increase of optically thick high frequency emission (before an optically thin flare) is the signature of plasmoid ejection, we consider the most straightforward interpretation of the light curves: the maximum of the optically thick emission at 8.3 GHz or 15 GHz signals the end of the event corresponding to the preponderance of plasma ejection. This is an important assumption in the following and we must look at it critically and within the context of the data available for these flares in partic-

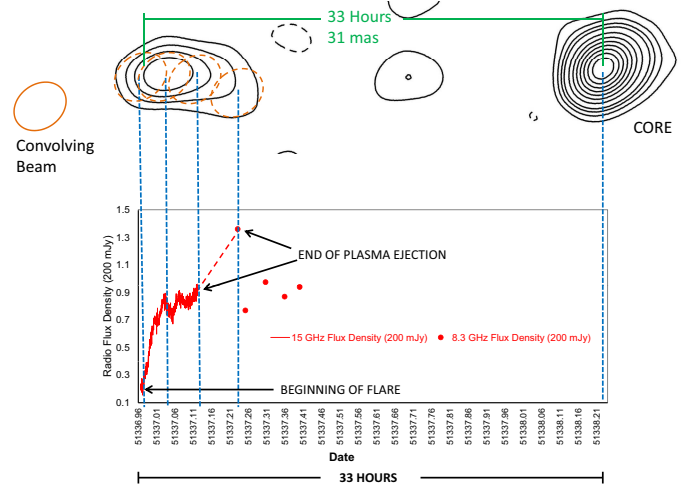


FIG. 13.— An 8.3 GHz VLBA image obtained 33 hours after flare initiation. The red curve is the 15 GHz flux density and the red dots are the 8.3 GHz flux density. The convolving beam used to process the image from the VLBA observation is the red closed curve with a size of 3.5 mas \times 3.1 mas. The contour levels relative to the peak flux of 32.2 mJy are at -5%, 5%, 10%, 20%, 30%, 40%, 50%, 60%, 70%, 80%, 90%. The radio image was generously provided by Vivek Dhawan. The emission between the core and ejection in the image is an artifact of the time variable core combined with sparse coverage in the u - v plane. See Section 2.2 for details.

ular. In general, one must note the following fundamental ambiguity. The attenuation due to optically depth evolves far more rapidly than adiabatic cooling as was shown in Punsly (2012). So, an optically thick plasma in a state of expansion that is becoming optically thin at a specific frequency may tend to increase in spectral luminosity even though there is no injection of energy (Moffet 1975). Furthermore, since the synchrotron self-absorption (SSA) optical depth is frequency dependent this can lead to a frequency dependent ambiguity to the end of the ejection. Yet since this process is distinct from the ejection process, it would typically be accompanied by a significant change in the rate of increase, curvature or slope of the radio light curve adjacent to its maximum. In order to explore the nature of the rise and the end of the ejection, we introduce three distinct types of light curves below as a means of exploring the issues raised above.

These concepts can be visualized in terms of the theoretical light curves that are presented in Figure 12. The type 1 light curve (on the left hand side of Figure 12) is the most common type in the sample described by Table 1. The discussion of equations (2) - (6) below indicate that there is only one reasonable interpretation of this light curve - some physical process (probably the ejection mechanism) ends abruptly. There is very little ambiguity in this instance. It should be noted that the SSA opacity is not typically that large in such a scenario when the light curve turns over. So changes in the attenuation occur at a much slower rate than changes in the radiative efficiency. This is evidenced by most of the light curves which often have relatively steep spectral indices (~ 0.5) between 2.3 GHz and 8.3 GHz when the high frequency light curve turns over (eg., Figures 3, 5, 6, 8, 9 and 11).

The decrease in the SSA optical depth resulting from plasmoid expansion can in principle be the dominant contributor to the luminosity increase near the maximum. This scenario is depicted in the middle light curve of Figure 12, the type 2 flare. The gradients in the light curve curvature near the maximum are distinct from a type 1 flare. A decrease in optical depth causes the luminosity of an expanding plasmoid to change gradually (semi-continuously). This has two manifestations not seen in the type 1 flare. The first is a flattening of the rise in the spectral luminosity light curve. The second is a gradual roll-over in the light curve at later times that transitions to a spectral luminosity decrease. These general characteristics of the curvature are independent of the detailed model of the rate of expansion and distribution of plasma.

The type 3 light curve is subtly different from the type 2 light curve (Figure 12). The physical mechanism responsible for this light curve is very different though. The first inflection point is the zeroth order realization of a drastic change in the ejection rate. This can be described as a powerful major ejection followed by a low level much weaker ejection that can last many hours, a "slow after burn". After which, the ejection shuts off and there is a rapid decrease in spectral luminosity as for the type 1 flare. Another difference between the type 2 and type 3 flares is that type 2 flares (based on the hypothesis of strong optical depth changes as the root cause of the spectral luminosity increase at 8.3 GHz) should be accompanied by very rapid and continual spectral index changes between 8.3 GHz and 2.3 GHz. By contrast, the spectral index changes are much less during the late time portion of the rise in the light curve for type 3 flares, since there is continual low level injection of optically thick plasma.

What is particularly striking about most of the light curves in Figure 1 - 11 is the extremely linear rise in flux density. Excellent examples are the epochs 50590.15, 50967.20, 51003.07, 51270.33, 51336.97, 51536.63, 51602.51 - 7 out of the 11 epochs. Note that this linear increase combined with equation (1) is in conflict with a scenario of nearly instantaneous injection (i.e time scales for injection much shorter than the rise time). For an instantaneous ejection and free expansion, one would expect a much more rapid ($\sim t^3$) increase in the flux density after the flare initiates. It is also curious that 5 of the epochs show clear signs of a discontinuous change (an abrupt change on time scales less than one hour) in the light curve from a linear rise to an approximately linear decrease (see Figures 1, 3, 4, 8 and 9). This abrupt, almost discontinuous behavior that typifies \sim half of the flares is also not consistent with the adiabatic expansion of an instantaneous injection. One expects a gradual transition from rise to decay in the expanding instantaneous plasmoid injection scenario in general (Moffett 1975). It is possible for the light curve decline to appear rather abrupt if the plasmoid is "very small" and the peak frequency is "very high" in a pure adiabatic ex-

pansion (of an instantaneous injection) scenario as noted in Figure 1 of van der Laan (1966). However, there is a necessary consequence to assuming such small sizes and a "high" frequency light curve maximum to explain the abrupt changes seen in the 8.3 GHz light curves. Namely, the light curve maxima at lower frequency (that occur at later times) are of significantly lower flux density than the narrower, earlier, high frequency light curve maxima as noted in van der Laan (1966); Punsly (2012). But, this is not the case for the major flares in GRS 1915+105 as evidenced by the light curves in Figures 3, 4, 5, 8, 9, 10, and 11 in which the opposite occurs. The time delayed low frequency (2.3 GHz) light curve maxima have larger flux densities than the earlier, higher frequency light curve maxima (8.3 GHz). Thus, pure adiabatic expansion scenarios are at odds with the spectral evolution of the major flares. The observed spectral evolution is consistent with the notion that 8.3 GHz is too low of a frequency to be associated the peak frequency of the SSA spectrum in early stages of major flare evolution in GRS 1915+105 (when the plasmoid is "very small") as discussed in Punsly (2012). The fact that the light curve maxima increase in amplitude at lower frequency (contrary to adiabatic expansion) was shown to be a result of the radiative efficiency increasing, as the minimum energy condition is approached, during the December 1993 flares (Punsly 2012).

There is a simple explanation of this abrupt inflection in terms of a source that turns off. To see this, define the spectral luminosity in terms of the total volumetric efficiency (which includes the effects of local emissivity and SSA optical depth), $\epsilon_{total}(t)$ and the total internal energy of the plasma (magnetic and leptonic), $E_{total}(t)$,

$$L_\nu(t) \equiv \epsilon_{total}(t)E_{total}(t) . \quad (2)$$

For most flares it is verified that there is an approximately linear increase after the start time, t_0 , which we model in a simple mathematical form

$$L_\nu(t) = A(t - t_0) , \quad (3)$$

where A is a constant. The total energy as a function of time can be described by a source, $Q(t)$ (injected power) and a sink $S(t)$ (i.e radiation losses, expansion losses).

$$E_{total}(t) = \int_{t_0}^t Q(T) - S(T) dT . \quad (4)$$

Combining Equations (2) - (4) one finds

$$L_\nu(t) = A(t - t_0) = \epsilon_{total}(t) \int_{t_0}^t Q(T) - S(T) dT , \quad t < t_o \quad (5)$$

For the numerous type I flares in Table 1, there is an abrupt change in the functional form of the light curve at $t = t_1$ (as discussed earlier in this section) which we model in a simple mathematical form

$$L_\nu(t) = A(t_1 - t_0) - B(t - t_1) = \epsilon_{total}(t) \left[\int_{t_0}^{t_1} Q(T) - S(T) dT - \int_{t_1}^t Q(T) - S(T) dT \right] , \quad (6)$$

where B is a constant. There is no straightforward physical reason for $\epsilon_{total}(t)$ or $S(t)$ to change abruptly (eg., in the case of instantaneous injection) since synchrotron cooling, expansion losses and SSA opacity changes due to adiabatic expansion are gradual (Moffet 1975). Thus, the straightforward solution is that $Q(t > t_1) \ll Q(t < t_1)$, ie. the source has virtually shutoff. This does not eliminate more elaborate scenarios as viable, but since there is a simple direct interpretation of the data, we consider it reasonable, and look for more corroboration of this interpretation below in the VLBA data. As another note on this calculation, for type III flares this argument applies to the second inflection point in the light curves. As for the first inflection point, it suggests that $Q(t)$ decreases significantly, but not to almost zero.

The abrupt cutoff from $Q(t)$ shutting off will produce a change in the light curve independent of frequency by Equation (6). Although the shape of the light curve around this inflection point might be affected by the SSA opacity. For the type II flares the profile is strongly affected by the frequency dependent SSA opacity making the exact time of the source turnoff difficult to extricate from the light curve. Hence, all type II flares carry an uncertainty in the flare end date in Table 1 and the type I flares do not.⁵

It is worth noting an additional complication that can potentially make the light curve interpretation as one of the three types a little bit ambiguous. After the major ejection, there can be strong optically thick shocks in the plasmoid (Dhawan et al 2004). Furthermore, it was found in Punsly (2012) that there are often multiple ejections of compact components that radiate spectra that are peaked at high frequency. They are sufficiently weak that by the time they become optically thin at low frequency, they are too weak to be segregated from other weak sources in the system. If there are strong oscillations near the end of the flare rise (eg., Figures 2 and 7) then this creates significant uncertainty in the estimate of the end of the plasma injection for that major flare.

We consider an anecdotal example closely in order to check the details of our light curve surrogate for determining plasma ejection durations. Fortunately, there is excellent data for the flare that initiates at epoch 51336.970. Figure 13 shows a VLBA 8.3 GHz image taken 33 hours after the start of the flare that is superimposed on the radio light curve. The center of the radio core is placed at 33 hours after the flare initiation on the horizontal axis of the plot. The "radio jet" is directed towards the flare start to show its formation in a time reversed sense. In order to see if the regions of peak flux density correspond to the rise of the optically thick flux, we assume that the plasmoid propagation speed is constant since inception. This was shown to be the consistent with the time snapshots in other ejections imaged with VLBA and MERLIN (Dhawan et al 2000). So it is a reasonable assumption to implement here. Thus, the length of the jet on the sky plane can be used as a ruler in time, a linear transformation of the time axis, T , to

the angular separation from the core in the sky plane, AS . The simple formula, for the time of ejection from the core is $T = AS/V$ where $V = (31 \text{ mas} / 33 \text{ hours}) = 0.94 \text{ mas} / \text{hour}$ (which is just the propagation speed of the jet on the sky plane). The closed contours superimposed on the image in Figure 13 represent the convolved beam-width that is used to create the image and can be considered the resolution limit of the image. Amazingly, the strong peaks in the flux density correspond with the rise in the 15 GHz flux density in the light curve. The weak tail (jet) corresponds to the slight rise in the 8.3 GHz flux density seen after this in the light curve. It is unclear if this slight rise in the optically thick 8.3 GHz flux and the weak tail is more ejected plasma or just back flow (in the frame of the plasmoid) from MHD (magneto-hydrodynamic) induced viscosity at the outer boundary of the advancing plasmoid (eg., Kelvin-Helmholtz and Rayleigh-Taylor instabilities) or back reflecting shocks from the plasmoid interface with the interstellar medium as expected from the method of characteristics (Sanders 1983). This perfect alignment of the light curve and the VLBA image may or may not be coincidental.

Even taking a pessimistic view that the alignment in the figure is coincidental, one can still ask what the figure indicates. Because of the extrapolation from the end of the 15 GHz rise to the 8.3 GHz point in the light curve is very steep, one does not know if the rate of increase of optically thick flux flattened out around 51337.100 or not. The abrupt change in the 8.3 GHz light curve after 51337.231 seems to indicate a distinct change in the plasma dynamics. This is the maximum viable time for the end of significant plasma ejection based on an analysis of the light curve only and seems to be indicated by the VLBA image also. Therefore, the radio image seems to independently corroborate the idea that there is no major plasma ejection after the light curve has peaked or has flattened out - we use the radio image to corroborate the maximum limit on the the length of time plasma ejection that is listed in Table 1.

The radio image can be used to shed some light on the estimation of the lower range of the duration for the plasma to be ejected. The 15 GHz light curve rises at a constant steep rate until it reaches a local maximum at 51337.031. This aligns perfectly with the peak of the VLBA image. However, the rise is also steep from 51337.100 and 51337.120. Thus, there seems to be significant plasma ejection during this time interval as well. There is no clear evidence that the 15 GHz light curve is flattening out at this point as it would be doing if it were dominated by expansion effects (i.e., there is insufficient data to distinguish between a type 2 or type 3 light curve). The interpretation of an increase in ejected plasma is consistent with the VLBA image, since the detected flux in the image at the corresponding time is based on contours that are 3 and 4 times the noise level (as indicated by the magnitude of the negative contour). The radio image supports the notion that a significant if not the majority of the plasma was injected before 51337.031. But, it would be an enormous extrapolation of the existing data to assume that the entire flux was ejected during this time interval and all the extended structure in the VLBA is entirely a consequence of the MHD effects spreading out the plasma distribution as discussed above.

⁵ The flare model in Section 3 and in Punsly (2012) is not the shock model of Marscher and Gear (1985) which can create sharp inflection points in the light curve by adjusting the numerous free parameters (Turler et al 2000). If the background jet is destroyed during the ejection as indicated in Dhawan et al (2004), there is no jet for the shock to propagate along.

At a minimum, the figure bounds the flare rise time between the end of the rise of the 15 GHz light curve and the peak of the 8.3 GHz for this flare. We do not expect the interpretation of the light curve shape to be significantly different for the other flares. In general, we carry this uncertainty in the end of the flare rise time in all of our calculations.

3. IMPLICATIONS OF THE OPTICALLY THIN LOW FREQUENCY RADIO EMISSION

The implementation of low frequency radio flux (~ 151 MHz - 408 MHz) to estimate the energy content of the plasma within radio lobes has a rich tradition in the study of radio loud AGN (Rawlings and Saunders 1991; Willott et al 1999; Blundell and Rawlings 2000; Punsly 2005). The low frequency is chosen to eliminate significant contributions due to the optically thick emission (synchrotron-self absorbed emission) from the radio core. The fundamental uncertainties in the application of these methods to GRS 1915+105 are, (Fender et al 1999a; Punsly 2012),

1. Is the plasma protonic or positronic?
2. What is the minimum electron energy, E_{min} ($E_{min} = 1$ in units of the electron rest mass energy, $m_e c^2$)?
3. There is uncertainty in the size of the region that produces the bulk of the radio emission. The size of the physical region that produces the preponderance of the radio emission in major flares appears to be smaller than the FWHM (full width at half maximum) beamwidth of the VLA, VLBA or MERLIN interferometers (Rodriguez and Mirabel 1999; Dhawan et al 2000; Fender et al 1999a).
4. Is the minimum energy or the equipartition assumption justified?

3.1. Method of Estimating the Power Required to Eject Major Flares

There are significant uncertainties listed above, many of which are ameliorated in a method developed in Reynolds et al (2009). The modeling method exploits the fact that synchrotron self-absorbed plasmoids are restricted in physical dimension by the shape of their spectrum. In particular, the frequency and the width of the spectral peak. This provides two added pieces of information beyond the spectral index and flux density of the optically thin high frequency tail. Such an analysis provides strong constraints on the size of the emitting region. In order to implement the modeling method, one must have sufficient frequency coverage so that the peak and the high frequency tail of the spectrum are defined. Furthermore, the data must be quasi-simultaneous because strong flares evolve rapidly, especially in their compact self-absorbed phase. A literature search revealed one such instance of broadband simultaneous frequency coverage in Rodriguez et al (1995) for a flare in December 1993. The modeling of the self-absorbed components of this powerful flare and their time evolution was studied

in detail in Punsly (2012). The insight provided by the fortuitous monitoring of this very compact and powerful flare motivates the assumption that the low frequency optically thin radio emission should be a robust estimator of the ejected plasma energy for other flares if it is used in conjunction with knowledge of when the flare evolved from optically thick to optically thin.

The relevant aspect of GRS 1915+105 discussed in Punsly (2012) was the time evolution of the compact flares which greatly enhances the accuracy of already insightful methods of plasmoid energy estimates developed in Reynolds et al (2009) and resolves most of the ambiguity noted at the beginning of this section. The fact that the flares were very compact and strong allowed for a very slow evolution of the synchrotron self absorption (on the order of a few days). This facilitated adequate time resolution to deduce the following behavior. The flares emerged optically thick. The 15 GHz - 22 GHz emission rose because of the injected energy and became enhanced as the ejected plasmoid became less optically thick to synchrotron self absorption as it expanded. Eventually the plasma became optically thin, even between 1.4 GHz and 2.3 GHz. Physically, the plasmoid began very far from equipartition and was magnetically dominated and positronic in composition. As it expanded, it evolved toward equipartition and the minimum electron, $E_{min} \approx 1$. Around the time that the optically thin flux at 2.3 GHz was near a maximum, the plasmoid was close to equipartition.

Our basic assumption is the following: the detailed modeling of the time evolution of the flares from December 1993 can be used as a template for the time evolution of other plasmoids that evolve far more rapidly and have sparser low frequency radio coverage. The energy in the ejected plasmoids in this paper are estimated by a method that is based on the optically thin 2.3 GHz flux density. It is important to emphasize the optically thin character for two reasons. First, for strong flares the 2.3 GHz flux sometimes peaks when the flare is still optically thick at 2.3 GHz and secondly the estimate on plasmoid size will only be valid near the peak optically thin flux at low frequency. In particular, we know the time evolution is one which begins with a synchrotron self-absorbed optical depth of $\tau(2.3 \text{ GHz}) \gg 1$, corresponding to an attenuation factor of $e^{-\tau} \ll 1$. As the plasmoid expands, the $\tau(2.3 \text{ GHz})$ decreases and is less than unity when it is optically thin at this frequency. Based on the models in Punsly (2012), one expects $\tau(2.3 \text{ GHz}) \approx 0.1$ when the flux reaches its peak value.

The calculation proceeds as in Punsly (2012) and Reynolds et al (2009) with two equations that must be solved simultaneously. The first is an equation for the optical depth,

$$\tau(2.3 \text{ GHz}) \equiv \mu(\nu = 2.3 \text{ GHz})R = 0.1, \quad (7)$$

where $\mu(\nu)$ is the synchrotron self-absorption (SSA) attenuation coefficient (see equation (14), below) and R is the radius of the plasmoid. The second equation is the flux density at 2.3 GHz when $\tau = 0.1$, $S_{\nu=2.3 \text{ GHz}}(\tau = 0.1)$, that can be approximated from our knowledge of plasmoid evolution in Punsly (2012) as

$$S_{\nu=2.3\text{GHz}}(\tau = 0.1) \approx \text{peak optically thin flux density at 2.3 GHz} . \quad (8)$$

Equations (7) and (8) are solved simultaneously in a time snapshot when the evolving plasmoid composition of the major flares in Punsly (2012) is characterized by the constraints

1. the plasma is primarily positronic
2. the plasma is near a minimum in energy
3. $E_{min} \approx 1$.

The solution is unique.

To convert these equations to the physical parameters in the plasmoid, we assume a power-law energy distribution for the relativistic electrons,

$$N(E) = N_{\Gamma} E^{-n} , \quad (9)$$

where the radio spectral index $\alpha = (n - 1)/2$ and E is the energy of the electrons in units of $m_e c^2$. Consider the leptonic thermal energy density, U_e , and the magnetic field energy density, U_B . Equation 9 with condition 3

above yields

$$U_e \approx m_e c^2 \frac{N_{\Gamma}}{n - 2} , \quad (10)$$

and

$$U_B = \frac{B^2}{8\pi} , \quad (11)$$

The total energy density stored in the leptonic plasma is given by

$$U = U_B + U_e . \quad (12)$$

If V is the volume of the plasmoid, in the approximately uniform limit, we define the total plasmoid energy as

$$E_{\text{total}} \approx UV . \quad (13)$$

To implement equation (7), we take the standard result for the SSA attenuation coefficient in the plasma rest frame (noting that $\nu = \nu_o/\delta$) from Reynolds et al (1996); Ginzburg and Syrovatskii (1969),

$$\mu(\nu_o) = \frac{3^{\alpha+1} \pi^{0.5} g(n) e^2 N_{\Gamma}}{8 m_e c} \left(\frac{eB}{m_e c} \right)^{(1.5+\alpha)} \nu_o^{-(2.5+\alpha)} \delta^{(2.5+\alpha)} , \quad (14)$$

$$g(n) = \frac{\Gamma[(3n+22)/12] \Gamma[(3n+2)/12] \Gamma[(n+6)/4]}{\Gamma[(n+8)/4]} . \quad (15)$$

The Doppler factor, δ , is given in terms of Γ_{rel} (not to be confused with the gamma function in the expression above), the Lorentz factor of the outflow; β , the three velocity of the outflow and the angle of propagation to the line of sight, θ ; $\delta = 1/[\Gamma_{\text{rel}}(1 - \beta \cos \theta)]$ (Lind and Blandford 1985). In order to describe the total energy in equation (13) in terms of observable quantities, we need to express the spectral luminosity in terms of observed flux density. One can express the observed flux density, $S(\nu_o)$, in the optically thin region of the spectrum using the relativistic transformation relations from Lind and Blandford (1985),

$$S(\nu_o) = \frac{\delta^{(k+\alpha)}}{4\pi D_L^2} \int j'_{\nu} dV' , \quad (16)$$

where D_L is the luminosity distance and j'_{ν} is emissivity evaluated in the plasma rest frame at the observed frequency. The constant k is of geometrical origin and is 3 for unresolved emission as is the case here. To make the connection between the observed flux density in equations (8) and (16) to the local synchrotron emissivity within the plasma note that the synchrotron emissivity is given in Tucker (1975) as

$$j_{\nu} = 1.7 \times 10^{-21} (4\pi N_{\Gamma}) a(n) B^{(1+\alpha)} (4 \times 10^6 / \nu)^{\alpha} \quad (17)$$

$$a(n) = \frac{\left(2^{\frac{n-1}{2}} \sqrt{3} \right) \Gamma \left(\frac{3n-1}{12} \right) \Gamma \left(\frac{3n+19}{12} \right) \Gamma \left(\frac{n+5}{4} \right)}{8\sqrt{\pi} (n+1) \Gamma \left(\frac{n+7}{4} \right)} . \quad (18)$$

Our solution is a numerical iterative method that solves equations (7) - (18) simultaneously under the assumption of a spherical volume. Without any knowledge to the contrary, we assume spherical and homogeneous since the plasmoids are too small to be resolved (Punsly 2012). Per condition "2" above, the parameters (N, B, R) are optimized until a solution to equations (7) to (18) with the minimum energy is found. This is considered the physical solution and its parameters are displayed in Table 2.

3.2. Estimating the Number Density Spectral Index

For a given kinematically determined δ , the one unknown in the equations above is the number density spectral index, n . This is determined from α of the optically thin component. First, one must subtract the flux density of the optically thick core. We cannot use the baseline flux density in Figures 1 - 11 to estimate this quantity because the core jet gets disrupted during the ejection and re-establishes itself at a different level after the ejection stops (Dhawan et al 2000, 2004). Since there is uncertainty associated with this quantity, we estimate the spectral index in the presence of background core flux by two different methods that we describe below.

The first method assumes that the random variations in the 8.3 GHz light curve that occur after the flare has risen to its peak represent optically thick time variations

of the core. This estimation is computed by first performing a linear fit to the 8.3 GHz flux density over a 3 to 5 hour period. The magnitude of the standard deviation of the residuals from the linear fit to the data are considered to be the time averaged radio core flux density at 8.3 GHz (flat spectrum: $\alpha = 0$ is assumed). The second column of Table 2, n_{rms} , lists the estimated values of n that are based on this method. The average of our 8 estimated values is $n_{rms} = 2.60$. For the epochs 50590.16, 51270.33, 51535.63 there is not enough data sampling to use this method and the sample average is used as a default value.

A second method uses the spectral index of the optically thin emission at late times in the flare, α . The late time aspect is important because it allows sufficient time for the large instabilities in the core flux (corona and disk) to decay and strong shocks in the ejected plasmoid to be damped as well. The inherently longer time scales facilitate discrete time averaging that also diminishes said effects. An important aspect that was discovered in Punsly (2012) that holds true for the models presented here is that the leptons responsible for the 2.3 GHz to 8.3 GHz emission are at fairly low energy for relativistic astrophysical ejecta (with E equal to a few tens at most). The important consequence is that there is minimal spectral ageing due to synchrotron losses in the time frames considered, thus the spectral index is indicative of n for low energy leptons (where most of the energy resides), even at earlier times. Thus, estimating α in the optically thin emission at late times is both a critical and relevant aspect of the calculation.

Ideally, we would want VLBA maps of the core at both frequencies at the time of the estimate of α . Unfortunately, we only have this for one flare, that of 51336.970, as shown in Figure 13. The next best option is to fit the data at late times for 2.3 GHz, 8.3 GHz and 15 GHz with a two component model. The core component in the model is chosen to have a flat spectrum $\alpha \approx 0$ from 2.3 GHz to 15 GHz and one then solves for the spectral index of the optically thin flux component and the normalization of the two power law components. The three flux density data points and the three unknowns provide a unique solution. For strong major flares, the late time behavior, one to three days after launch, make the method viable since the optically thin flux level is well above the random optically thick background of the time variable core and emission from strong shocks⁶. The weak major flares, 50590.16, 51270.33 can not be extricated from the background fluctuations and the sample average of $n_2 = 2.80$ is used in Table 2. The same value is chosen for 51535.63 for which there is insufficient data to make an estimate.

The n values that are estimated from the spectral method above are listed as n_2 in column 3 of Table 2. The range of n in columns 2 and 3 can be used as an estimate of our uncertainty in n in the following. The first

⁶ The weak major flares described above are defined by ~ 100 - 200 mJy of peak optically thin flux density at 2.3 GHz. The stronger major flares are those that are defined to be above this level and can achieve optically thin flux densities exceeding 1500 mJy (Rodriguez et al 1995). The strong major flares are of sufficient strength that they are clearly distinguished from other background radio emission. In the following, the word "major" will often be dropped in the flare designations of weak and strong.

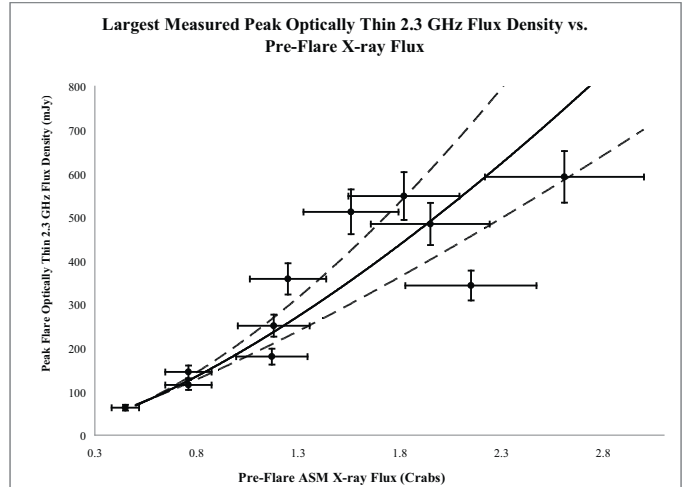


FIG. 14.— A weighted least squares powerlaw fit (solid black curve) to the X-ray fluxes 0 to 4 hours before the flares (in Crabs) and the peak optically thin measured 2.3 GHz flux densities (mJy). The dashed curves indicate the standard error in the fit from the first row of Table 5. The errors on the flux densities are simply the uncertainty in the GBI measurements are from Table 1.

column of Table 2 is the estimated flare initiation date. The last two columns are the estimated energy within the ejecta, E_{plasmoid} , and the time averaged power required to launch the ejecta (Q), respectively.

3.3. Doppler Factor Considerations

The solutions depend strongly on the distance to the source D through its role in the determination of δ (see the entries in Table 2). The intrinsic kinematics of apparent superluminal motion are a very strong function of D (Fender et al 1999a). Thus it was important to solve for the plasmoid energy in a plausible range of D and δ . In order to estimate the Doppler factors we assume that the kinematic results from Fender et al (1999a) are common to the entire time frame from 1997 to 2000 as evidenced by interferometric observations of multiple flares (Dhawan et al 2000; Miller-Jones et al 2005). The values of δ for different values of D are listed in Table 2 and the model based estimates of the energy and Q were computed accordingly. From equation (16), the *intrinsic* spectral luminosity associated with an observed flux density $\sim \delta^{-(3+\alpha)}$. For example, if the distance to the source is 10.5 kpc instead of 11 kpc, the intrinsic spectral luminosity changes by a factor $\sim (0.31/0.54)^{3.9} = (1/8.7)$. Thus, the strong dependence of the energy on δ and D that is depicted in Table 2 - a change in distance from 11 kpc to 10.5 kpc reduces the energy of the plasmoid by a factor of 5 - 6.

3.4. Explicit Computation and Comparison to Other Minimum Energy Estimates

This section is a discussion of the nuances of this method as compared to conventional minimum energy estimates. This highlights some of the advantages of the method and illustrates the details of how a calculation is performed in practice. An instructive example is the flare at epoch 50750.50 for which a standard minimum energy estimate was performed with an assumed distance 11 kpc in Fender et al (1999a).

The calculational method described above has two assumptions. One is that all major flare ejections are considered to have approximately the same Doppler factor (and we explore a range of possible distance dependent fixed Doppler factors in Table 2). Secondly, the plasmoids are of similar origin and composition as those in December 1993 and they will evolve similarly. Thus, the plasmoid will be near peak optically thin flux density at 2.3 GHz when it evolves toward $\tau = 0.1$ and a minimum energy configuration. The system is self consistently solved for with equations (7) to (18). Given our two assumptions, the uncertainty in our estimation of the energy in the plasmoid is contained in two quantities, n and $S_{\nu=2.3\text{GHz}}(\tau = 0.1)$. The range of plausible values of $S_{\nu=2.3\text{GHz}}(\tau = 0.1)$ are determined by the light curve in Figure 2 and are listed in column 5 of Table 1. To quantify an uncertainty in n we use the two methods described in section 3.2 (listed in columns (2) and (3) of Table 2) to create a plausible range. First, we consider the RMS variations from a linear fit to the data after the rise of the flare has terminated. We consider the 8.3 GHz data from the GBI observing run that started at 50750.83 and ended at 50751.07. A linear fit of the flux density in mJy versus date yields an intercept of 7874.645 and a slope of -0.15516. The data was then subtracted from the linear fit. The standard deviation of the residuals was computed which yielded an RMS variation of 11 mJy⁷. This was equated to the time averaged amplitude of an oscillating core flux density. The core was assumed to be flat spectrum, $\alpha = 0$, from 2.3 GHz to 8.3 GHz. The result was subtracted from the total flux density to yield the optically thin contribution

⁷ As a consistency check, the same calculation applied to the 15 GHz data a few hours earlier (the strong oscillations in Figure 2)

to the ejection at each epoch of observation. The two point spectral indices of the plasmoid from 2.3 GHz to 8.3 GHz were then averaged over the observation, yielding $\alpha = 0.573$ for the optically thin component. Bearing in mind that the points sampled overlap the time frame for which $\tau = 0.1$, we corrected the flux for SSA to get the intrinsic spectral index of 0.65. The corresponding $n_{rms} = 2.30$ is listed in column 2 of Table 2.

The second estimate of n from Table 2, n_2 , requires estimates of the core, weak compact ejecta and optically thick shock emission at late times in the flare evolution. To determine these contributions, we average the flux densities at both 2.3 GHz and 8.3 GHz from 50754.825 to 50755.023 (12 points). The 15 GHz Ryle data slightly precedes the GBI data and we average this flux density from 50754.791 to 50754.808. The time averaged flux densities are 148 mJy, 54 mJy and 35 mJy at 2.3 GHz, 8.3 GHz, and 15 GHz, respectively. Our two component model yields $\alpha = 0.84$ or $n = 2.68$ for the optically thin component and a background flat spectrum flux density of 6 mJy with $\alpha = 0$.

The errors in the parameters needed for our calculation are defined by

$$0.65 \leq n \leq 0.84, \quad (19)$$

$$431\text{mJy} \leq S_{\nu=2.3\text{GHz}}(\tau = 0.1) \leq 548\text{mJy}. \quad (20)$$

From the range of input parameters given by Equations (19) and (20), we compute the minimum energy state for $\tau = 0.1$ for the four configurations at the vertices of the rectangular range of 2-D parameter space defined by n and $S_{\nu=2.3\text{GHz}}(\tau = 0.1)$:

yields a time averaged core flux density of 15 mJy

$$E_{\text{plasmoid}}[n = 0.65, S_{\nu=2.3\text{GHz}}(\tau = 0.1) = 431\text{mJy}] = 2.13 \times 10^{42}\text{erg/s}, \quad (21)$$

$$E_{\text{plasmoid}}[n = 0.65, S_{\nu=2.3\text{GHz}}(\tau = 0.1) = 548\text{mJy}] = 2.84 \times 10^{42}\text{erg/s}, \quad (22)$$

$$E_{\text{plasmoid}}[n = 0.84, S_{\nu=2.3\text{GHz}}(\tau = 0.1) = 431\text{mJy}] = 4.05 \times 10^{42}\text{erg/s}, \quad (23)$$

$$E_{\text{plasmoid}}[n = 0.84, S_{\nu=2.3\text{GHz}}(\tau = 0.1) = 548\text{mJy}] = 5.40 \times 10^{42}\text{erg/s}. \quad (24)$$

The estimated energy and its error are then given by the mean and standard deviation of the numbers above, $E = 3.61 \times 10^{42} \pm 1.42 \times 10^{42}$ ergs.

In order to calculate the power required to eject the plasma we write

$$Q = \Gamma_{rel} E_{\text{plasmoid}} / (T_{end} - T_{start}), \quad (25)$$

where the relativistic Lorentz factor at 11 kpc is given by Fender et al (1999a) as $\Gamma_{rel} = 5$. T_{start} and T_{end} are the plasma ejection start and stop times from Table 1,

$$T_{start} = 50750.52 \pm 0.02, \quad T_{end} = 50750.695 \pm 0.055. \quad (26)$$

Thus, from Equation (25)

$$Q = 5(3.61 \times 10^{42}\text{ergs}) / (0.175\text{ days}) \pm Q \sqrt{\left(\frac{\delta E_{\text{plasmoid}}}{E_{\text{plasmoid}}}\right)^2 + \left(\frac{\delta T_{end}}{T_{end} - T_{start}}\right)^2 + \left(\frac{\delta T_{start}}{T_{end} - T_{start}}\right)^2}, \quad (27)$$

where the error is from the quadrature propagation of

error: $\delta E_{\text{plasmoid}}$, δT_{end} , δT_{start} are the errors in the en-

ergy (above), start and end times, respectively. From Section 2.1, a minimum error that can be assigned to both δT_{start} and δT_{end} is $0.1(T_{end} - T_{start})$ and this error is added in quadrature to any other uncertainty to the flare initiation time and end times that are indicated in Equation (26). In this particular case, equations (24) - (27) yield $Q = 1.19 \times 10^{39} \pm 6.29 \times 10^{38}$ ergs/s, one of the largest relative errors in the sample. The uncertainty induced by the uncertainty in the distance to the source (as imprinted through the Doppler factor) is accounted for by the three rows for each for each flare in Table 2, corresponding to distances of 10 kpc, 10.5 kpc and 11 kpc (Doppler factors 0.31, 0.54 and 0.69, respectively).

We highlight some key differences in this estimation technique and a standard minimum energy estimate in Fender et al (1999a).

- It is noted in Fender et al (1999a) that the plasmoid size is uncertain and it was assumed that the radius of the plasmoid is 6.5×10^{14} cm. By contrast, this calculation has one assumption: the plasmoids are of similar origin and composition as those in December 1993 and they will evolve similarly. Thus, the plasmoid will be near peak optically thin flux density at 2.3 GHz when it evolves toward $\tau = 0.1$ and a minimum energy configuration. The system is self consistently solved for with equations (7) to (18). The uncertainties in our estimated n and $S_{\nu=2.3\text{GHz}}(\tau = 0.1)$ lead to a range of calculated plasmoid radii $1.75 \times 10^{14}\text{cm} < R < 1.95 \times 10^{14}$ cm that are derived in the self-consistent solutions that are defined by equations (7) - (18). The stored energy in the plasmoid $\sim R^{9/7}$ (Fender et al 1999a). Thus, the ratio of the two energy estimates is $\approx (6.5/1.85)^{9/7} = 5.1$. This explains the fact that Fender et al (1999a) computes an energy of 2×10^{43} ergs and in Table 2 we find $(3.61 \pm 1.42) \times 10^{42}$ ergs. In relation to this, note that the range of $S_{\nu=2.3\text{GHz}}(\tau = 0.1)$ in Equation (20) and the light curve in Figure 2 indicate that the calculation is performed in the interval 50750.83 and 50751.01. From equation (26) this indicates a time frame for plasmoid expansion of 26000 sec to 44000 sec in our models. This equates to a lateral expansion velocity between 0.13c and 0.25c. By contrast there is an implicit $\approx c$ expansion speed in the Fender et al (1999a) analysis since the flux density that they use in the calculation (550 mJy) is at epoch 50750.86 in combination with their aforementioned radius. The MERLIN observations in Fender et al (1999a) were interpreted as providing an upper limit on the expansion speed of 0.14c. VLA and VLBA monitoring have been used to estimate an expansion speed of $\approx 0.2c$ (Dhawan et al 2000). Thus, the self-consistent time evolutionary model presented here is the more consistent with observation.
- Fender et al (1999a) choose a plasma injection episode of 12 hours to convert E_{plasmoid} to Q . Our analysis of the plasma start and stop times indicate an energy injection time of ≈ 4 hours.
- The power required to eject the plasmoid in Fender

et al (1999a) is 2×10^{39} ergs/sec compared to $Q = 1.19 \times 10^{39} \pm 6.29 \times 10^{38}$ ergs/s found above. There are two competing effects. The Fender et al (1999a) estimate is a factor of ≈ 5 larger for the large assumed radius in the first item above, and a factor of ≈ 3 smaller for longer rise time (second item) for a net $\approx (5/3)$ increase from our estimate.

This example was perhaps the most complicated case considered, The same techniques for estimation of quantities and errors are applied to the other (simpler) energy and Q estimates in columns 6 and 7 of Table 2, respectively.

4. RXTE X-RAY FLUX

In order to make a connection between the accretion flow state before and during the major ejections, one needs X-ray observations that cover a wide range of energies as there is a significant contribution to the intrinsic luminosity from the black body energies of ~ 1 keV and a corona with significant luminosity up to ~ 50 keV or more (Done et al 2004; Fuchs et al 2003; Rodriguez et al 2008b). Apriori, one cannot assume that one particular range of energies is more connected to the production of major flares than another as the physics of the accretion flow and flare production are basically unknown. Thus, the broadest possible X-ray coverage is required to make any significant conclusions. As discussed in the Introduction, the ejections occur unexpectedly on the order of hours so there is no time for target of opportunity X-ray observations just before the flare starts and during the rise, all data is serendipitous. Thus, there must be the densest possible survey time sampling in combination with fortunate circumstances. During the period that was considered, the only viable alternative is the All Sky Monitor (ASM) of the Rossi X-ray Timing Explorer (RXTE). The data is not sufficient to produce spectra and only covers a very narrow range of energies, 1.2 keV to 12 keV. The ASM light curves are provided in counts/sec so it would be advantageous to

1. convert count rates to fluxes
2. convert observed flux to intrinsic (unabsorbed) flux
3. extend the estimated measured flux from the range 1.2 keV to 12 keV to 1.2 keV to 50 keV
4. find methods for ameliorating systematic errors in the ASM count rates in individual bins in the data that is provided by the ASM team.

The final result is an estimator that takes the counts measured in the three bins of the ASM data, 1.2–3 keV, 3–5 keV and 5–12 keV, and converts this to an intrinsic (unabsorbed) X-ray luminosity from 1.2–50 keV. Our calibrations indicate a final result with an intrinsic error of less than 15%, assuming a constant absorption column density.

4.1. The ASM Data Measured in Crabs

The first step in our process was to convert the ASM count rates to Crab units and use the archival Crab spectra to later convert this to fluxes. This initial effort had

TABLE 2
ESTIMATES OF POWER REQUIRED TO EJECT MAJOR FLARES

Estimated Flare Start (MJD)	n_{rms}	n_2	D ^b kpc	δ ^c	E_{plasmoid} 10^{42} ergs	Q 10^{38} ergs/s
50590.160	2.60	2.80	11	0.31	0.32 ± 0.08	4.55 ± 1.27
50590.160	2.60	2.80	10.5	0.54	0.066 ± 0.017	0.60 ± 0.16
50590.160	2.60	2.80	10	0.69	0.031 ± 0.008	0.22 ± 0.06
50750.520	2.30	2.68	11	0.31	3.61 ± 1.42	12.80 ± 6.29
50750.520	2.30	2.68	10.5	0.54	0.78 ± 0.28	1.55 ± 0.83
50750.520	2.30	2.68	10	0.69	0.37 ± 0.13	0.57 ± 0.29
50916.140	2.78	2.92	11	0.31	11.70 ± 3.07	19.34 ± 5.71
50916.140	2.78	2.92	10.5	0.54	2.05 ± 0.62	2.10 ± 0.71
50916.140	2.78	2.92	10	0.69	1.00 ± 0.27	0.80 ± 0.24
50967.200	2.40	2.80	11	0.31	4.70 ± 2.97	20.9 ± 13.6
50967.200	2.40	2.80	10.5	0.54	0.99 ± 0.63	2.73 ± 1.78
50967.200	2.40	2.80	10	0.69	0.47 ± 0.30	0.99 ± 0.65
51003.070	2.76	2.84	11	0.31	2.60 ± 0.31	9.01 ± 1.69
51003.070	2.76	2.84	10.5	0.54	0.51 ± 0.07	1.10 ± 0.22
51003.070	2.76	2.84	10	0.69	0.24 ± 0.03	0.40 ± 0.08
51270.330	2.60	2.80	11	0.31	1.07 ± 0.24	5.16 ± 1.82
51270.330	2.60	2.80	10.5	0.54	0.24 ± 0.06	0.73 ± 0.29
51270.330	2.60	2.80	10	0.69	0.11 ± 0.03	0.26 ± 0.10
51336.970	2.74	2.88 ^a	11	0.31	5.79 ± 0.97	16.34 ± 4.24
51336.970	2.74	2.88 ^a	10.5	0.54	1.22 ± 0.20	2.13 ± 0.55
51336.970	2.74	2.8 ^a	10	0.69	0.56 ± 0.08	0.76 ± 0.18
51375.150	2.62	2.96	11	0.31	1.81 ± 0.74	8.06 ± 3.44
51375.150	2.62	2.96	10.5	0.54	0.38 ± 0.15	1.06 ± 0.43
51375.150	2.62	2.96	10	0.69	0.18 ± 0.07	0.38 ± 0.15
51499.702	2.62	2.76	11	0.31	3.22 ± 0.71	10.77 ± 2.60
51499.702	2.62	2.76	10.5	0.54	0.89 ± 0.20	1.86 ± 0.44
51499.702	2.62	2.76	10	0.69	0.38 ± 0.09	0.61 ± 0.15
51535.630	2.60	2.80	11	0.31	5.23 ± 1.58	15.13 ± 4.86
51535.630	2.60	2.80	10.5	0.54	1.11 ± 0.33	1.99 ± 0.63
51535.630	2.60	2.80	10	0.69	0.52 ± 0.16	0.73 ± 0.23
51602.506	2.70	2.90	11	0.31	1.10 ± 0.23	5.07 ± 1.18
51602.506	2.70	2.90	10.5	0.54	0.23 ± 0.04	0.65 ± 0.14
51602.506	2.70	2.90	10	0.69	0.11 ± 0.02	0.24 ± 0.05

^aThere was a simultaneous a 2.3 GHz VLBA observation and a 8.3 GHz observation (see Figure 13). The core flux density was 21 mJy and 42 mJy at 2.3 GHz and 8.3 GHz, respectively (Vivek Dhawan private communication, 2012). Simultaneous GBI data indicated flux densities of 378 mJy and 146 mJy at 2.3 GHz and 8.3 GHz, respectively on 51338.23. Subtracting off the core flux density yields $\alpha = 0.94$ or $n = 2.88$.

^bdistance to source

^cDoppler factor compatible with kinematics and the distance to source in the previous column

some startling results which motivated the in-depth analysis and modeling that appeared in the previous section and the rest of this paper. We explored two methods of converting counts per second to Crabs. Firstly, we converted the counts/second (cts/s) from 1.2–12 keV to Crabs: 75.41 cts/s in the ASM band from 1.2–12 keV is the equivalent of 1 Crab. This conversion is based on the 16 year archival average of ASM data. But, since the Crab spectra are harder than the GRS 1915+105 spectra, it was more accurate in our final conversion to cgs flux units to convert the cts/s in each bin to Crabs separately then convert to a flux in each bin. The first method of using the whole ASM band overestimated the flux. We define the three ASM bins, 1.2–3 keV, 3–5 keV and 5–12 keV, as bin 1, bin 2 and bin 3, respectively. The counts rates in each bin are defined symbolically as

$$C1 \equiv \text{cts/s in bin 1} , \quad (28)$$

$$C2 \equiv \max(5.75, \text{cts/s in bin 2}) , \quad (29)$$

$$C3 \equiv \text{cts/s in bin 3} . \quad (30)$$

The lower limit in the expression for C2 arises from a systematic error that occurs in bin 2 sporadically. Sometimes at low count rates there is a "drop out" in this channel and count rates far below the much more accurate PCA archival count rate for this energy range are registered. This is clearly a systematic ASM error and the 5.75 cts/s are the equivalent of the lowest archival recorded PCA count rate based on a comparison between PCA and ASM using the flux conversion for ASM in equation (30b), below. This minimum cutoff is derived

and discussed in detail in Sections 4.2.1 and 4.2.4.

The archival ASM Crab count rates are very stable in each bin with only a few percent variation over the epochs that are considered in this treatment. Thus, we used the archival average count rates to convert the count rates in the three bins to fluxes in Crabs, $F_i(\text{Crab})$, $i = 1, 2, 3$, by the equations

$$F1(\text{Crab}) = C1/26.78 , \quad (31)$$

$$F2(\text{Crab}) = C2/23.25 , \quad (32)$$

$$F3(\text{Crab}) = C3/25.38 . \quad (33)$$

In order to compute the errors in each bin, we combined the errors for each of the GRS 1915+105 count rates with the mean error on the Crab count rate, and the variance of the Crab rate in each bin. We then propagated the errors as if they were independent. This independence is not formally true, but we consider this of small consequence since the variance in each bin is not that high, and the statistical errors on the rates are not that high either.

Figure 14 shows that the peak measured optically thin flux density at 2.3 GHz (column 6 of Table 1) is strongly correlated with the ASM X-ray flux in Crabs (computed from the entire ASM band). The Pearson (Spearman Rank) probability of the scatter occurring by random chance is 1.9×10^{-5} (5.2×10^{-3}). A weighted least squares powerlaw fit (with an index of 1.45 ± 0.17) is very good with only the one outlier, 50967.20, with the aforementioned large gap in GBI coverage near the peak of the optically thin flux density at 2.3 GHz (Reed 1989). The

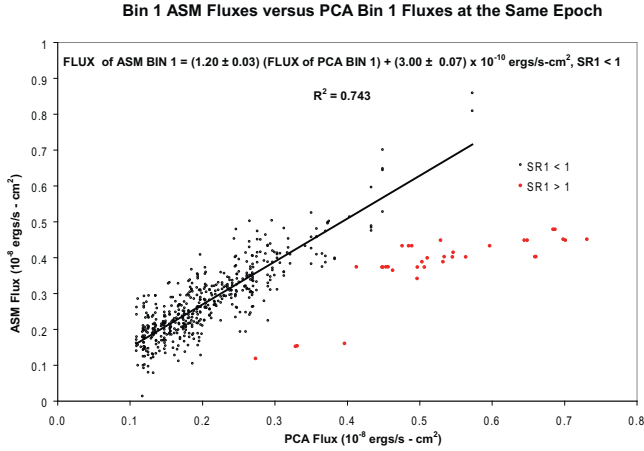


FIG. 15.— A comparison of bin 1 fluxes in quasi-simultaneous observations of ASM and PCA. The units on the axes are 10^{-8} ergs/sec/cm 2 . R^2 is the squared multiple regression coefficient.

fit improves somewhat if we use the estimated value of $S_{\nu=2.3\text{GHz}}(\tau = 0.1)$ from Table 1 since this is effectively an average flux density near the peak flux density and is less sensitive to gaps in the observations. The improved weighted least squares powerlaw fit has an index of 1.40 ± 0.11 . The probability that the data scatter occurs by random chance and the two quantities are not correlated is 0.26% according to a Spearman rank correlation test.

Figure 14 represents an empirical relationship between the X-ray flux 0 to 4 hours before the ejection of a flare and the peak optically thin low frequency flux of the flare. It is model independent. We believe this to be a fundamental property of the physics of major flare launching and it motivates the detailed model dependent analyses that follow. In its most transparent guise, these correlations seem to indicate a direct relationship between the luminosity of the accretion flow just prior to major flare ejection with the energy of the flare and/or the power required to launch the flare.

4.2. Converting ASM Bin Counts to X-ray Luminosity

Thusly motivated, we develop the physical interpretation of the ASM data. The physical meaning of Figure 14 would be greatly enhanced if the ASM fluxes in Crabs could be related quantitatively to the broadband energy

⁸ We call these softness ratios so they are not confused with the various definitions in the literature of flux ratios that are designated as hardness ratios

⁹ e.g. http://heasarc.gsfc.nasa.gov/docs/xte/pca_news.html#practices

released as X-rays by the accretion flow. This effort is challenged by the extrinsic and intrinsic sources of absorption and the narrow range of energies detected by ASM. This is a large extrapolation of the data and its success is not guaranteed ahead of time. We show that for a wide range of X-ray spectral states that estimators with an accuracy on the order of 15% are achieved. This endeavor requires that all the information in the ASM bins must be used and the results must be verified by comparison to a large database of quality models of quasi-simultaneous broadband PCA observations. The ASM data not only give fluxes, but the ratios of the fluxes in the various bands contain information on the spectral slope that can be used to extrapolate the energies higher than those that are observed.

4.2.1. Converting ASM Crab Fluxes to cgs Units

As a first step in this process, it is useful to define softness ratios in terms of fluxes in the three ASM bins ⁸. The first step is to convert Crab fluxes to cgs fluxes. To do so, we downloaded, reduced and analyzed all RXTE/PCA observations of the Crab nebula performed between 1996 February, 1 (MJD 50114) and 2011 December, 31 (MJD 55926).

The RXTE/PCA data were reduced following standard steps (e.g. (Rodriguez et al 2008b)) with the HEASOFT v6.12 to obtain spectra and response matrices. GTI were defined following the recommended filter criteria ⁹. We then extracted source and background spectra from the top layer of PCA/Proportional Counter Unit #2, using the bright source background model, while the response matrix was produced with accordance to the gain epochs of the PCA. The resultant spectral products were loaded into XSPEC v12.7.1 and fitted.

As we wanted to obtain fluxes in well defined bands, we fitted the spectra with a simple power law model, only ensuring that the reduced χ^2 was less than 1.8 for the fit (and fluxes) to be acceptable. This resulted in about 500 'good' fits. As the Crab spectrum was fairly constant during the epochs spanned by the flares in Table 1 (most of the apparent changes over time were due to epoch changes and compensated for by taking the appropriate matrices), the fluxes in the 1.5–3 keV, 3–5 keV, 5–12 keV, 12–50 keV were then obtained by taking the mean over the whole period of observations.

$$F1 = F1(\text{Crab})(1.05 \times 10^{-8})\text{ergs/s} - \text{cm}^2 = C1(3.92 \times 10^{-10})\text{ergs/s} - \text{cm}^2, \quad (34)$$

$$F2 = F2(\text{Crab})(0.731 \times 10^{-8})\text{ergs/s} - \text{cm}^2 = C2(3.14 \times 10^{-10})\text{ergs/s} - \text{cm}^2, \quad (35)$$

$$F3 = F3(\text{Crab})(1.17 \times 10^{-8})\text{ergs/s} - \text{cm}^2 = C3(4.61 \times 10^{-10})\text{ergs/s} - \text{cm}^2, \quad (36)$$

where the right hand side of the expressions is derived

from Equation (29). In regards to the definition in equa-

tion (28b) for C2, the minimum observed PCA flux between 3 keV and 5 keV is $\approx 1.8 \times 10^{-9}$ ergs/s $- \text{cm}^2$ except for a small handful of anomalous outliers that could be artifacts of observational errors or data reduction. Equation (30) represents the flux calibration of the ASM count rates.

4.2.2. The Database of PCA Spectra Used to Calibrate the ASM Estimator of Luminosity

It is desirable to convert the observed fluxes in the three bins to a broadband (unabsorbed) intrinsic flux from 1.2–50 keV which is directly representative of the physical state of the accretion flow of GRS 1915+105. This requires extrapolating the flux beyond 12 keV to 50 keV and de-reddening the fluxes. The program for accomplishing this will be based on comparisons of ASM observations with PCA observations that are simultaneous to within 45 minutes. The PCA data has sufficient spectral coverage and sensitivity that model fits to the data can be performed that allow us to estimate the absorption on the line of sight for the various bins and detailed intrinsic spectral parameters. In order to permit a high fidelity comparison of the PCA and the ASM data that are asynchronous by as much as 45 minutes requires that the PCA fluxes of the chosen epochs be stable over similar time scales. This will also permit higher signal to noise spectra.

In Belloni et al (2000), the spectral states of GRS 1915+105 were categorized in 12 classes. This is based on the PCA light curves and color-color diagrams. From this classification one can see that there are 2 stable classes on time scales > 1 second. These are the χ and ϕ classes. These more or less correspond to the two stable sets of hard and soft states that we found in the PCA data for GRS 1915+105 that were suitable for modeling because of their stability. In terms of ASM data these PCA selected states also turn out to be distinct. To see this, consider, the notion of softness ratios defined from equation (31)

$$SR1 = F1/F2 = 0.93(C1/C2) , \quad (37)$$

$$SR2 = F2/F3 = 0.68(C2/C3) . \quad (38)$$

The soft states lie at SR2 values above the line

$$SR2 = 1.15(SR1) + 0.28 , \quad (39)$$

in the SR1-SR2 plane and the hard states lie at SR2 values below this line. The concept of bin based fluxes that are used in equations (31) and (32) apply to PCA data if we make designations analogous to equation (29),

$$F1(PCA) \equiv \text{flux in bin 1} , \quad (40)$$

$$F2(PCA) \equiv \text{flux in bin 2} , \quad (41)$$

$$F3(PCA) \equiv \text{flux in bin 3} , \quad (42)$$

$$F4(PCA) \equiv \text{flux in bin 4} . \quad (43)$$

Where PCA(bin 2) and PCA(bin 3) are the same as for ASM, 3–5 keV and 5–12 keV, respectively. PCA(bin1) is narrower than for ASM, 1.5–3 keV. PCA(bin4) is not covered by ASM observations, 12–50 keV. We found 630 hard (χ) states and 164 soft (ϕ) states.

The spectra were fitted with a model consisting of (absorbed) thermal Comptonization and a Gaussian to account for a fluorescent iron line. N_H was fixed to

$5.7 \times 10^{22} \text{cm}^2$, (see (Belloni et al (1997); Munro et al (1999); Rodriguez et al (2008b))), since leaving it free to vary leads in many occurrences of unphysical values. Good fits (with a reduced $\chi^2 < 1.8$) was achieved for 501 spectra¹⁰. This does not mean that the other spectra are "bad". This means that our simple model is not able to approximate, or does not represent, the spectrum well enough so that we can trust the fluxes obtained with it. These extra 20% of the spectra probably need extra components such as disk and/or additional power laws to achieve a reliable fit.

4.2.3. Systematic Difference in ASM and PCA Data

Before we can implement the use of an estimator for the ASM data, we must understand the differences between measured ASM and PCA fluxes (derived from count rates for ASM per equation (29)). We were able to find systematic differences by finding quasi-simultaneous pairs of ASM and PCA observations for our sample of 501 hard PCA spectra. We found 531 pairs of observations that were simultaneous to within 45 minutes. The large number of pairs arises because more than one ASM observation can be within 45 minutes of a PCA observation. We note three major issues

1. Bin 1 for ASM is wider than bin 1 for PCA, 1.2–3 keV as opposed to 1.5–3 keV
2. As noted in regards to equations (28) and (29), there is a "drop out" effect in the ASM data in bin 2 for low count rates that occurs unpredictably
3. Considering the entire archive of PCA observations, SR1 is rarely greater than 1 ($\ll 1\%$) and in these rare cases it is just slightly above 1. Yet $SR1 > 1$ about 29% of the time in the ASM database with such large values and frequency that it is unlikely to be explained solely by items (1) and (2) above. It is not clear how much item (2) contributes to this, so we must assume that this is an independent instrumental effect and a source of uncertainty in the ASM data. We compared large SR1 epochs from ASM to quasi-simultaneous PCA data taken $\sim 10 - 30$ minutes separated in time when the source was in what appeared to be a steady state. The PCA softness ratios were generally modest and "typical" for the source.

In order to assess item (1) above, we created a scatter plot of the flux in bin 1 for quasi-simultaneous ASM observation with the flux in bin 1 for the corresponding PCA observations. The results are plotted in Figure 15. The fit to the scatter plot only represents epochs with $SR1 < 1$ in the ASM data-set. The plot indicates that assuming 20% more flux would replicate expanding the PCA bin 1 from 1.5–3 keV to the range of 1.2–3 keV. This is the method that we will use to compensate for the bin size difference in our comparison of PCA and quasi-simultaneous ASM data.

Interestingly, the 33 $SR1 > 1$ epochs have a disjoint distribution concentrated toward the lower right of the

¹⁰ None of the soft state observations are coincident or close in time to a superluminal ejection so we do not consider them further here.

TABLE 3
X-RAY LUMINOSITY EVOLUTION (BASED ON $D = 11$ KPC)

24 Hour Baseline Date MJD	Baseline Date (MJD)	Pre-Flare Date (MJD)	24 Hour Baseline L_{24hr} (10^{39} ergs/s)	Baseline L_{5-10hr} (10^{39} ergs/s)	Pre-Flare $L_{pre-flare}$ (10^{39} ergs/s)	Average Rise L_{rise} (10^{39} ergs/s)	Baseline 5 - 12 keV Flux (10^{-8} ergs/s- cm^2)	Pre-Flare 5 - 12 keV Flux (10^{-8} ergs/s- cm^2)	Average Rise 5 - 12 keV Flux (10^{-8} ergs/s- cm^2)
50589.093	50590.090	50590.157	0.39 ± 0.05	0.40 ± 0.05	0.41 ± 0.05	0.35 ± 0.05 ^b	0.65 ± 0.7	0.66 ± 0.06	0.57 ± 0.06 ^b
50749.356	50750.284	50750.351	0.50 ± 0.07	0.84 ± 0.12	1.05 ± 0.15	0.71 ± 0.1	2.25 ± 0.23	2.94 ± 0.29	1.63 ± 0.16
50915.091	50916.024	50916.146 ^a	0.47 ± 0.06	0.61 ± 0.07	1.36 ± 0.18	1.15 ± 0.15	1.39 ± 0.14	3.91 ± 0.39	3.35 ± 0.34
50915.091	50916.024	50916.089 ^a	0.47 ± 0.06	0.61 ± 0.07	1.28 ± 0.18	1.17 ± 0.15	1.39 ± 0.14	3.79 ± 0.38	3.35 ± 0.34
50966.101	50966.908	50967.148	0.41 ± 0.06	0.50 ± 0.07	1.19 ± 0.17	1.03 ± 0.15	1.01 ± 0.1	3.72 ± 0.37	3.03 ± 0.30
51001.912	51002.770	51002.907	0.42 ± 0.06	0.52 ± 0.07	0.76 ± 0.11	0.45 ± 0.06	1.36 ± 0.14	1.94 ± 0.19	0.85 ± 0.09
51269.314	51270.250	51270.315	0.46 ± 0.06	0.58 ± 0.07	0.54 ± 0.07	...	1.31 ± 0.13	1.21 ± 0.12	...
51335.942	51336.870	51336.940	0.41 ± 0.06	0.80 ± 0.10	1.07 ± 0.14	0.89 ± 0.12	1.85 ± 0.19	2.88 ± 0.29	2.54 ± 0.25
51373.967	51374.962	51375.099	0.43 ± 0.06	0.69 ± 0.09	0.71 ± 0.09	0.55 ± 0.07	1.54 ± 0.15	1.81 ± 0.18	1.32 ± 0.13
51498.555	51499.415	51499.614	0.52 ± 0.07	0.57 ± 0.08	0.79 ± 0.11	...	1.22 ± 0.12	1.72 ± 0.17	...
51534.490	51535.422	51535.556	0.43 ± 0.06	0.56 ± 0.08	0.90 ± 0.13	...	1.15 ± 0.12	2.33 ± 0.23	...
50610.410	N/A	51602.361	0.50 ± 0.07	...	0.60 ± 0.09	1.15 ± 0.06	...

^aThere is very little difference in the measured fluxes on 50916.146 and 50916.089, so the uncertainty in the flare initiation time from Table 1 does not create significant uncertainty in our results.

^bIncludes epoch 50590.16 for which some X-ray observations exist within a range spanned by the 10% uncertainty that was assigned to all flare start time estimates in Section 2.1

plot in Figure 15. The implication is that $SR1 > 1$ ASM measurements are systematically different than other epochs and need to be treated as such. It is unclear how much of this difference is due to intrinsically large soft fluxes (i.e., a very bright disc) during these epochs in combination with the softer ASM bins or a consequence of the aforementioned instrumental effect. The vast majority of observations with $SR1 > 1$ in ASM are very luminous hard steady states that are characterized by an elevated soft flux in the quasi-simultaneous PCA observations (see Figure 15). The flux excess above the PCA sample average is largest in bin 1 (86% above the sample average) decreasing with each more energetic bin, so that the bin 4 fluxes are approximately the sample average. It turns out that the $SR > 1$ states are rather common just before and during flares (see Table 4), so it is desirable to be able to estimate the luminosity accurately in this situation. Not knowing why errors occur in ASM measurements during these luminous states, we conclude that the best way to deal with this dichotomy is by treating the systematic differences in $SR1 > 1$ and $SR1 < 1$ ASM epochs, empirically; i.e. fit the data separately in a way that compensates for potential systematic errors in the ASM data. In practice, this empirical method for dealing with item 3 is to segregate the $SR1 > 1$ epochs and fit them to the PCA data as an independent data

set.

The method of dealing with item 2 was discussed earlier with regards to equations (28) and (29). The lowest recorded PCA flux in bin 2 is 1.8×10^{-9} ergs/sec/cm². This will be treated as a minimum allowed value for an ASM flux in bin 2. As such, any ASM measurement lower than this is very uncertain with only a lower limit of 1.8×10^{-9} ergs/sec/cm² designated. This uncertainty must be compensated for empirically by the choice of the estimator that minimizes the error associated with this expedience. In general, we had sufficient data from observations just before or just after an observation for which we had to invoke the minimum cutoff in equation (28b) that afforded us the luxury of being able to exclude these data from our analysis. The lone exception is epoch 51002.907 since this data (with equation (28b) applied) is the only available data that is close in time to the flare start.

4.2.4. The ASM Estimator of Intrinsic X-ray Flux

Using the strategy described in the previous section for dealing with systematic difference between ASM and PCA bin data, we obtained the following estimator, F_0 of $F_{intrinsic}$ (the intrinsic, unabsorbed flux derived from PCA models) based on ASM count rates

$$F_0 = 0.561 \left[(4.363F1(SR1)^{0.2772}) + (1.3767F2(SR1)^{0.0255}) + F3(1 + 2.730e^{-(2.114SR2)}) \right] + 1.25 \times 10^{-8} \text{ergs/s/cm}^2, \quad SR1 < 1, \quad (44)$$

$$F_0 = 0.478 \left[(4.363F1(SR1)^{0.2772}) + (1.3767F2(SR1)^{0.0255}) + F3(1 + 2.730e^{-(2.114SR2)}) \right] + 1.08 \times 10^{-8} \text{ergs/s/cm}^2, \quad SR1 > 1, \quad (45)$$

There are many potential sources of errors in the estimator: the data, the models as well as error induced by variability and time offsets in the ASM and PCA data sampling. Instead of making assumptions about the manner

in which the error propagates, we empirically determine the error by direct comparison of the estimator with the flux from the modeled PCA data. The relative error σ for the estimator in equations (34) and (35) is computed

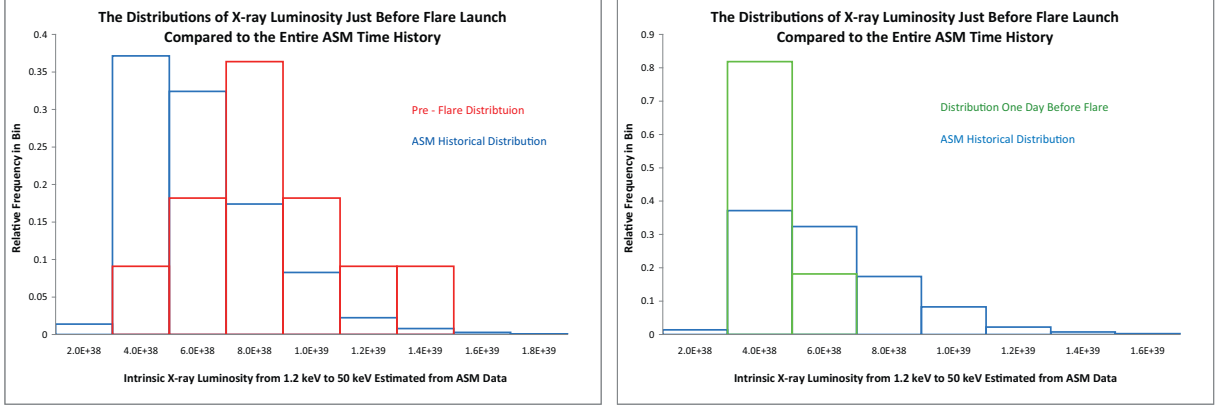


FIG. 16.— Left panel: the distribution of the intrinsic X-ray luminosity 0 to 4 hours before a major flare is ejected compared to the archival distribution of intrinsic X-ray luminosity that is estimated from the entire ASM archive. Right panel: the distribution of the intrinsic X-ray luminosity one day before a major flare is ejected compared to the archival distribution of intrinsic X-ray luminosity that is estimated from the entire ASM archive. The luminosity tends to be elevated just prior to the flare ejection as opposed to being relatively low a day before. The plots assume $D = 11$ kpc.

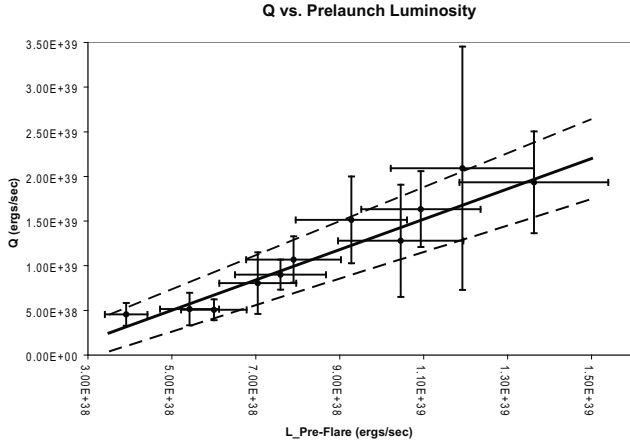


FIG. 17.— Estimated time average power of the flare ejection, Q , (Table 2) vs X-ray luminosity 0 to 4 hours before a major flare ejection (from Table 3). The solid black line is the weighted least squares fit from Table 5. The dashed black lines indicate the standard error to the fit from Table 5. A strong correlation is obvious (see text).

as the standard deviation of the difference, $F_{\text{intrinsic}} - F_0$

$$\sigma \left(\frac{F_{\text{intrinsic}} - F_0}{F_{\text{intrinsic}}} \right) = 0.131, \quad SR1 < 1, \quad (46)$$

$$\sigma \left(\frac{F_{\text{intrinsic}} - F_0}{F_{\text{intrinsic}}} \right) = 0.143, \quad SR1 > 1, \quad (47)$$

The empirical fit in equations(34) and (35) has a strange functional form as a consequence of fitting the four PCA bins in equation (33), separately as a preliminary step. These expressions are not unique nor are they aesthetically beautiful but they do reproduce the PCA modeled data accurately as evidenced by equations (36) and (37).

Figures 1 - 11 plot the (unabsorbed) intrinsic X-ray luminosity, $L_{\text{intrinsic}}(1.2-50)$, light curves based on formulas in equations (34) -(37) and a distance of 11 kpc. The intrinsic luminosity light curves typically do not have the extreme variations of the raw Crab flux light curves that appears in the same plots. This seems to indicate that

the intrinsic luminosity is considerably less variable than would be assumed by just looking at raw ASM count rates, in general.

4.3. X-ray Properties Before and During Flares

The formulas in equations (34) - (37) are used to estimate the 1.2 keV to 50 keV intrinsic X-ray luminosity, $L_{\text{intrinsic}}(1.2-50)$, just before and the time averaged luminosity during flares ($L_{\text{pre-flare}}$, L_{rise} , hereafter). The results and the associated errors are compiled in Table 3. A fiducial distance of 11 kpc is chosen for the table. Column (3) is the date of the closest RXTE observation to the start of the major ejection that is obtained from Figures 1 - 11 and is previously tabulated in Table 1. Column (2) is the ASM observation with a date that precedes the pre-flare X-ray date in column (3) that is closest in time with a time difference of at least one hour. We call this a (local) baseline from which the pre-flare flux varies ($L_{5-10\text{hr}}$, hereafter). It is close enough in time to be plausibly causally connected to the pre-flare X-ray luminosity. In column (1) we look at ASM observations to establish another more distant baseline, the luminosity 24 hours ($L_{24\text{hr}}$, hereafter) before the pre-flare RXTE observation of column (3). This may or may not be causally connected. The luminosity in columns (4) - columns (7) are computed from equations (34) - (37). ASM observations during the actual rise of the flares exist for only 6 epochs. The ASM fluxes tend to be extremely time variable during the rise of the flares, so a time average is computed in column (7). The last 3 columns tabulate the hardest flux detected by ASM, bin 3. Counts were converted to flux with equation (30c).

We list the conclusions that are drawn from the results in Table 3.

1. Columns (6) and (7) of Table 3 indicate that the time averaged X-ray luminosity decreases during the plasmoid ejection, even though it is highly variable with strong peaks that can exceed the pre-flare levels.
2. Columns (6) and (7) of Table 3 indicate that L_{rise} , is correlated with $L_{\text{pre-flare}}$ (see Table 5).

TABLE 4
X-RAY SPECTRAL EVOLUTION

Baseline ^a Date	Pre-Flare Date	Baseline ^a SR1	Pre-Flare SR1	Average Rise SR1	Baseline ^a SR2	Pre-Flare SR2	Average Rise SR2
50590.090	50590.157	0.61	0.63	0.54 ^b	0.70	0.60	0.60 ^b
50750.284	50750.351	1.49	0.86	1.33	0.20	0.40	0.34
50916.024	50916.146	0.66	0.54	1.77	0.52	0.54	0.20
50966.908	50967.148	0.66	0.84	1.59	0.55	0.32	0.31
51002.770	51002.907	0.61	2.42	0.63	0.43	0.10	0.50
51270.250	51270.315	0.64	0.61	...	0.46	0.48	...
51336.870	51336.940	2.79	2.49	1.68	0.11	0.11	0.20
51374.962	51375.099	1.61	0.62	0.54	0.31	0.39	0.47
51499.415	51499.614	0.73	2.33	...	0.49	0.2	...
51535.422	51535.556	0.79	2.48	...	0.44	0.13	...
N/A	51602.361	...	0.46	0.61	...

^aThe local baseline is the ASM observation closest in time to the pre-flare observations, occurring at least one hour earlier.

^bIncludes epoch 50590.16 for which some X-ray observations exist within a range spanned by the 10% uncertainty that was assigned to all flare start time estimates in Section 2.1

- $L_{\text{pre-flare}}$ is significantly elevated relative to the archival distribution of X-ray luminosity for GRS 1915+105. A Kolmogorov-Smirnov test shows that $L_{\text{pre-flare}}$ tends to be of larger values than would be expected if they were representative of the distribution of luminosity that is derived from the complete ASM database of GRS 1915+105 observations at the 98.0% significance level. This is evident from the histogram in Figure 16.
- Columns (9) and (10) indicate a suppression of hard flux during plasma ejection. This might indicate a softening of the spectrum, but the ASM data is not good enough to determine this. The change in hard flux in of itself is insufficient to explain the preponderance of the decreased total flux during the flare rise.

Figure 16 is based on over 99.5% of the archival ASM database that satisfy the softness criteria in equation (32) for which the estimators in equations (34) and (35) are valid (over 76,000 epochs). In the bottom frame of Figure 16, we explore the postulate of Dhawan et al (2004) that a dip in the X-ray luminosity precedes the flare launch when the time scale defining the word "precede" is on the order of days. To this end, we compared $L_{24\text{hr}}$ (~ 30 hours before flare ejection) to the distribution of the ASM archival archive. A Kolmogorov-Smirnov test shows that the intrinsic luminosity 30 hours before flare launch is depressed relative to the archival distribution with a 96.9% statistical significance. What is particularly striking about this distribution is that every X-ray state 30 hours before flare ejection lies within a very narrow range of intrinsic X-ray luminosity, $\sim 4 - 5 \times 10^{38}$ ergs/s.

4.4. PCA Observations Near Flare Ejections

The closest RXTE/PCA observations (before) the onset of a major flare occurred on 51602.330–51602.361 for a flare start time 51602.506. GRS 1915+105 is in a class χ over the entire observation. The 1.5–50 keV unabsorbed flux is $\gtrsim 4.2 \times 10^{-8}$ erg/cm²/s indicating a rather bright occurrence for this class. This is, however, typical of the luminous "high hard states" or high plateau states mentioned in Fuchs et al (2003). We also note a slight decrease of the source unabsorbed flux over the last 2000 s of the observation.

We, also, explored the temporal properties of the source, verifying first through inspection of a dynamical

power density spectrum (PDS), that they were steady over the observation, as expected in a steady class χ observation (see e.g. Rodriguez et al. 2008b). We, then, extracted a PDS over the entire observation, and fitted it between 0.01 and 67 Hz. Above typically 20 Hz the PDS is consistent with white noise and was modeled with a constant with a value of 2.

A good fit was achieved with 4 Lorentzian (on top of the white noise), three of them with broad profile (one centered at 0 Hz), and a narrow feature indicative of the presence of a low frequency quasi-periodic oscillation (QPO). Inspection of the PDS, however, showed the presence of a slight residual (a kind of QPO shoulder) near the QPO. Adding another thin Lorentzian improved the fit significantly. The total RMS amplitude is 36.6 %. The QPO has a frequency of ~ 4.25 Hz and an RMS amplitude of ~ 6.7 %, while the additional feature has a frequency ~ 4.79 Hz and an RMS amplitude of ~ 4.7 %. Similar complicated QPO profiles have been seen in other sources (e.g. XTE J1859+226, Rodriguez and Varnière (2011) and references therein), and may indicate the inadequacy of Lorentzian fitting in specific cases. While the total RMS amplitude is rather usual for this type of class, we note that the QPO amplitude is, on the contrary, rather low, since class χ QPO can have amplitude of 10–15% (Rodriguez et al 2004).

We also consider the RXTE/PCA observation covering 51003.174–51003.2245 that occurs near the end of the injection episode (possibly after) corresponding to the flare 51003.07. GRS 1915+105 is also in a class χ over the whole observation. The 1.5–50 keV unabsorbed flux is 3.1×10^{-8} erg/cm²/s. The total RMS amplitude is ~ 43.7 % somewhat higher than in the previous observation. The PDS shows the presence of 2 QPOs harmonically related. The fundamental has a frequency of ~ 2.46 Hz and an RMS amplitude ~ 12.1 %, while its harmonic is at ~ 4.85 Hz and has an RMS amplitude ~ 5.0 %.

5. THE RELATIONSHIP BETWEEN X-RAY LUMINOSITY AND THE EJECTION POWER

The reason for developing the estimates of Q and $L_{\text{intrinsic}}(1.2 - 50)$ was to provide a physical insight into the the provocative correlation between pre-flare X-ray flux and peak optically thin flare 2.3 GHz flux density in Figure 14. In Table 5, we list all the potentially interesting correlations that we found. The first two columns X and Y are the variables for a weighted least squares

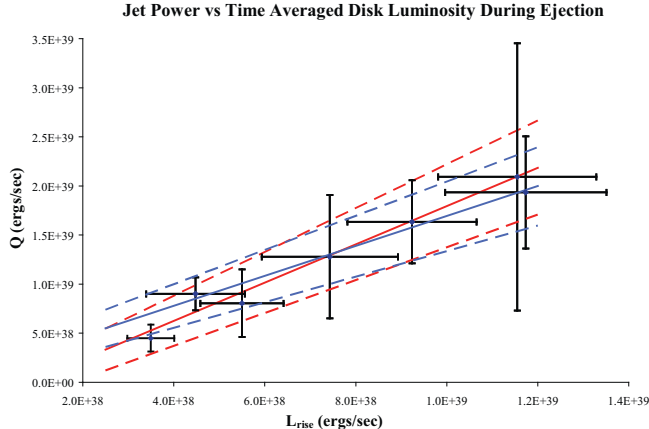


FIG. 18.— The correlation between the time averaged X-ray luminosity during a major flare ejection (from Table 3) and the estimated time averaged power required to eject the flare, Q , that is taken from Table 2. The solid blue line is the weighted least squares fit from Table 5. The dashed blue lines indicate the standard error to the fit from Table 5. The point at the far left of the plot represents epoch 50590.16. Formally X-ray observations precede the flare start time, but some X-ray observations exist within a range spanned by the 10% uncertainty that was assigned to all flare start time estimates in Section 2.1. The red lines indicate the fit with errors from Table 5 if the flare 50590.16 is included in the scatter plot, the blue lines are without flare 50590.16 included in the fit.

fit to $Y = mX + b$ with errors in both variables using the methods of Reed (1989). The estimated m and b are listed in columns 4 and 5. The next two columns are the correlation coefficients and the probability that the data scatter occurs by random chance.

The analog of Figure 14 in terms of physical estimates is Q as a function of $L_{\text{pre-flare}}$ that is plotted in Figure 17 with the data from Tables 2 and 3 and the curve fit and errors from Table 5. Notice from Table 5 that the correlation is much improved from Figure 14. The most direct indicator of the flare launch physics is L_{rise} . Unfortunately, there are only 6 major flares with X-ray data during launch. In spite of the small number statistics, the chance to probe this most fundamental indicator of the physics of major flare ejection makes it a worthwhile exercise to look for trends in the data. The X-ray light curves during flares is often highly time variable in Figures 1 - 11, similar to the post ejection X-ray state discussed in Trushkin et al (2007). By contrast, the estimators of flare energy and power in Section 3 are only time averages. Thus, we must use time averaged X-ray luminosity during the ejection, L_{rise} , in order to make relevant comparisons. This is affected by the aforementioned variability and the sparse and nonuniform time sampling during the brief flare rise. Thus, depending on the time sampling there can be significant uncertainty in this average that is best dealt with by larger samples. The scatter plot with the fits from Table 5 are plotted in Figure 18. Noting the strong variability in the X-ray luminosity in Figures 1 - 11 during flare launching, it seems likely that the instantaneous power required to launch the plasmoid is highly variable as well. This seems mirrored in the VLBA image in Figure 13 which is consistent with a strong abrupt burst (or bursts) followed by weaker ejecta. It is not known if these would appear in

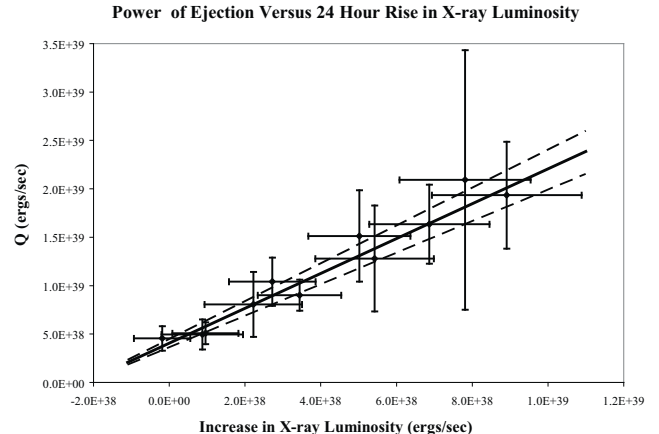


FIG. 19.— A plot of the correlation that exists between the increase in intrinsic X-ray luminosity one day preceding the ejection (from Table 3) and the estimated time averaged power of the ejection, Q . The plot is for the special case $D = 11$ kpc. The solid black line is the weighted least squares fit from Table 5. The dashed black lines indicate the standard error to the fit from Table 5.

or out of phase with the X-ray bursts without finer time resolution in the radio data sampling.

In Figure 19, we plot the increase in the $L_{\text{intrinsic}}(1.2 - 50)$ in the last day ($L_{\text{pre-flare}} - L_{24\text{hr}}$) preceding the plasma ejection (from Table 3) versus Q . There is a significant correlation that extends continuously to the weaker flares in which there is actually a decrease in luminosity before the ejection instead of an increase. The correlation in Figure 19 is redundant with that in Figure 17. It arises as a consequence of the fact that the X-ray luminosity one day before flare launch is confined to within a tight window as noted in regards to Figure 16, $\sim 4 - 5 \times 10^{38}$ ergs/s (see Table 3).

In summary, Tables 3 and 5 indicate the following evolution of the X-ray luminosity before and during flare launch. For the flares in our study, one day before the ejection, the system is in a low luminosity state with $L_{24\text{hr}} \sim 4 - 5 \times 10^{38}$ ergs/s. We find that major flares can be launched if the X-ray luminosity decreases or increases over the next 24 hours. The power and energy of the ejection scales with $L_{\text{pre-flare}}$. Our lone pointed observation, 3 to 4 hours before a major flare (epoch 51602.506), shows no spectral signature that indicates that an ejection is imminent. Table 3 and Figure 19 indicate that for strong flares $L_{\text{intrinsic}}(1.2 - 50)$ continues to increase from roughly a day before launch into the final hours preceding the ejection. From Table 5 when the flare is launched, the time averaged power, $Q + L_{\text{rise}}$, is highly correlated with $L_{\text{pre-flare}}$, with near equality if $D \approx 10.5$ kpc.

6. DISCUSSION

We have presented the most comprehensive possible study of the X-ray properties of GRS 1915+105 just prior to and during major flare ejection given the state of the available data. Our primary empirical result that is model independent is the strong correlation between the 1.2–12 keV X-ray flux 0 to 4 hours before a major flare ejection and the peak optically thin 2.3 GHz flux density of the flare. Most of the article was spent developing this result into one involving basic physical entities. In

TABLE 5
CORRELATION ANALYSIS

X	Y	D (kpc)	m slope ξ	b intercept ξ	Pearson Coefficient/ (Probability) ^c	Spearman Rank Coefficient/ (Probability) ^c	Figure
Log(X-ray Flux) ^d	Log[S] _a	...	1.45 ± 0.17	2.27 ± 0.04	0.938/(1.90 × 10 ⁻⁵)	0.879/(5.20 × 10 ⁻³)	14
Log(X-ray Flux) ^d	Log[S] _f	...	1.40 ± 0.11	2.31 ± 0.03	0.966/(1.28 × 10 ⁻⁶)	0.952/(2.60 × 10 ⁻³)	...
$L_{\text{pre-flare}}^b$	E_{plasmoid}^e	11	$7.37 \times 10^3 \pm 8.74 \times 10^2$	$-2.82 \times 10^{42} \pm 5.27 \times 10^{41}$	0.892/(2.20 × 10 ⁻⁴)	0.954/(2.60 × 10 ⁻³)	...
$L_{\text{pre-flare}}^b$	E_{plasmoid}^e	10.5	$1.71 \times 10^3 \pm 2.00 \times 10^2$	$-5.91 \times 10^{41} \pm 1.10 \times 10^{41}$	0.912/(9.32 × 10 ⁻⁵)	0.927/(3.20 × 10 ⁻³)	...
$L_{\text{pre-flare}}^b$	E_{plasmoid}^e	10	$8.75 \times 10^2 \pm 9.90 \times 10^1$	$-2.75 \times 10^{41} \pm 4.96 \times 10^{40}$	0.912/(9.32 × 10 ⁻⁵)	0.927/(3.20 × 10 ⁻³)	...
$L_{\text{pre-flare}}^b$	Q^b	11	1.70 ± 0.21	$-3.49 \times 10^{38} \pm 1.31 \times 10^{38}$	0.955/(4.81 × 10 ⁻⁶)	0.973/(2.00 × 10 ⁻³)	17
$L_{\text{pre-flare}}^b$	Q^b	10.5	0.24 ± 0.04	$-4.12 \times 10^{37} \pm 2.24 \times 10^{37}$	0.880/(3.51 × 10 ⁻⁴)	0.936/(3.00 × 10 ⁻³)	...
$L_{\text{pre-flare}}^b$	Q^b	10	0.10 ± 0.01	$-1.52 \times 10^{37} \pm 0.73 \times 10^{37}$	0.906/(1.22 × 10 ⁻⁴)	0.955/(2.60 × 10 ⁻³)	...
$L_{\text{pre-flare}}^b$	$Q + L_{\text{rise}}^b$	11	3.00 ± 0.33	$-8.60 \times 10^{38} \pm 2.99 \times 10^{38}$	0.955/(3.06 × 10 ⁻³)	0.886/(4.66 × 10 ⁻²)	...
$L_{\text{pre-flare}}^b$	$Q + L_{\text{rise}}^b$	10.5	1.41 ± 0.23	$-3.78 \times 10^{38} \pm 1.96 \times 10^{38}$	0.938/(5.62 × 10 ⁻³)	0.886/(4.66 × 10 ⁻²)	...
$L_{\text{pre-flare}}^b$	$Q + L_{\text{rise}}^b$	10	1.25 ± 0.19	$-3.06 \times 10^{38} \pm 1.50 \times 10^{38}$	0.955/(3.10 × 10 ⁻³)	0.886/(4.66 × 10 ⁻²)	...
$L_{\text{pre-flare}}^{b,j}$	$Q + L_{\text{rise}}^{b,j}$	11	2.35 ± 0.24	$-2.15 \times 10^{38} \pm 1.59 \times 10^{38}$	0.952/(9.61 × 10 ⁻⁴)	0.893/(2.86 × 10 ⁻²)	...
$L_{\text{pre-flare}}^{b,j}$	$Q + L_{\text{rise}}^{b,j}$	10.5	0.99 ± 0.15	$1.09 \times 10^{37} \pm 9.49 \times 10^{37}$	0.937/(1.82 × 10 ⁻³)	0.929/(2.26 × 10 ⁻²)	...
$L_{\text{pre-flare}}^{b,j}$	$Q + L_{\text{rise}}^{b,j}$	10	0.87 ± 0.13	$1.63 \times 10^{37} \pm 7.85 \times 10^{37}$	0.944/(1.38 × 10 ⁻³)	0.929/(2.26 × 10 ⁻²)	...
L_{rise}^b	E_{plasmoid}^e	11	$8.09 \times 10^3 \pm 2.49 \times 10^3$	$-1.57 \times 10^{42} \pm 1.49 \times 10^{42}$	0.775/(6.99 × 10 ⁻²)	0.886/(4.66 × 10 ⁻²)	...
L_{rise}^b	E_{plasmoid}^e	10.5	$1.72 \times 10^3 \pm 4.51 \times 10^2$	$-2.82 \times 10^{41} \pm 2.46 \times 10^{41}$	0.820/(4.59 × 10 ⁻²)	0.886/(4.66 × 10 ⁻²)	...
L_{rise}^b	E_{plasmoid}^e	10	$9.11 \times 10^2 \pm 2.17 \times 10^2$	$-1.30 \times 10^{41} \pm 1.17 \times 10^{41}$	0.872/(1.18 × 10 ⁻²)	0.886/(4.66 × 10 ⁻²)	...
$L_{\text{rise}}^{b,j}$	$E_{\text{plasmoid}}^{e,j}$	11	$1.04 \times 10^4 \pm 2.05 \times 10^3$	$-3.14 \times 10^{42} \pm 1.00 \times 10^{42}$	0.832/(2.01 × 10 ⁻²)	0.929/(2.26 × 10 ⁻²)	...
$L_{\text{rise}}^{b,j}$	$E_{\text{plasmoid}}^{e,j}$	10.5	$2.40 \times 10^3 \pm 4.80 \times 10^2$	$-7.13 \times 10^{41} \pm 2.26 \times 10^{41}$	0.869/(1.11 × 10 ⁻²)	0.929/(2.26 × 10 ⁻²)	...
$L_{\text{rise}}^{b,j}$	$E_{\text{plasmoid}}^{e,j}$	10	$9.12 \times 10^2 \pm 2.54 \times 10^2$	$-2.49 \times 10^{41} \pm 8.70 \times 10^{40}$	0.907/(4.76 × 10 ⁻³)	0.929/(2.26 × 10 ⁻²)	...
L_{rise}^b	Q^b	11	1.52 ± 0.22	$1.68 \times 10^{38} \pm 1.36 \times 10^{38}$	0.980/(5.95 × 10 ⁻⁴)	0.886/(4.66 × 10 ⁻²)	18
L_{rise}^b	Q^b	10.5	0.20 ± 0.03	$2.62 \times 10^{37} \pm 1.88 \times 10^{37}$	0.931/(6.89 × 10 ⁻³)	0.772/(8.36 × 10 ⁻²)	...
L_{rise}^b	Q^b	10	0.08 ± 0.01	$8.50 \times 10^{36} \pm 6.05 \times 10^{36}$	0.949/(3.77 × 10 ⁻³)	0.886/(4.66 × 10 ⁻²)	...
$L_{\text{rise}}^{b,j}$	$Q^{b,j}$	11	1.95 ± 0.28	$-1.55 \times 10^{38} \pm 1.43 \times 10^{38}$	0.984/(6.23 × 10 ⁻⁵)	0.929/(2.26 × 10 ⁻²)	18
$L_{\text{rise}}^{b,j}$	$Q^{b,j}$	10.5	0.27 ± 0.05	$-2.04 \times 10^{37} \pm 2.24 \times 10^{37}$	0.948/(1.13 × 10 ⁻³)	0.857/(3.58 × 10 ⁻²)	...
$L_{\text{rise}}^{b,j}$	$Q^{b,j}$	10	0.11 ± 0.01	$-6.53 \times 10^{36} \pm 7.68 \times 10^{36}$	0.961/(5.76 × 10 ⁻⁴)	0.929/(2.26 × 10 ⁻²)	...
ΔL_{6hr}^h	Q^b	11	2.22 ± 0.33	$5.95 \times 10^{38} \pm 8.32 \times 10^{37}$	0.937/(6.33 × 10 ⁻⁵)	0.915/(6.00 × 10 ⁻³)	...
ΔL_{6hr}^h	Q^b	10.5	0.31 ± 0.07	$8.25 \times 10^{37} \pm 1.54 \times 10^{37}$	0.864/(1.28 × 10 ⁻³)	0.891/(7.40 × 10 ⁻³)	...
ΔL_{6hr}^h	Q^b	10	0.12 ± 0.03	$2.93 \times 10^{37} \pm 5.09 \times 10^{36}$	0.893/(5.02 × 10 ⁻⁴)	0.927/(5.20 × 10 ⁻³)	...
ΔL_{24hr}^i	Q^b	11	1.79 ± 0.16	$4.05 \times 10^{38} \pm 4.29 \times 10^{37}$	0.973/(5.32 × 10 ⁻⁷)	0.964/(2.20 × 10 ⁻³)	19
ΔL_{24hr}^i	Q^b	10.5	0.25 ± 0.04	$5.48 \times 10^{37} \pm 9.49 \times 10^{36}$	0.893/(2.16 × 10 ⁻⁴)	0.918/(3.60 × 10 ⁻³)	...
ΔL_{24hr}^i	Q^b	10	0.12 ± 0.01	$1.68 \times 10^{37} \pm 3.66 \times 10^{36}$	0.921/(5.65 × 10 ⁻⁵)	0.936/(3.00 × 10 ⁻³)	...
$L_{\text{pre-flare}}^b$	L_{rise}^b	k	1.16 ± 0.19	$-3.57 \times 10^{38} \pm 1.72 \times 10^{37}$	0.955/(2.73 × 10 ⁻³)	0.943/(3.48 × 10 ⁻²)	...
$L_{\text{pre-flare}}^{b,j}$	$L_{\text{rise}}^{b,j}$	k	0.84 ± 0.12	$-3.79 \times 10^{37} \pm 9.01 \times 10^{37}$	0.953/(8.93 × 10 ⁻⁴)	0.964/(1.78 × 10 ⁻²)	...

^aPeak observed $S_{\nu=2.3\text{GHz}}$ in mJy

^bergs units

^cProbability of occurring by random chance

^dCrab units

^eThe energy of the ejected plasmoid in ergs

^fEstimated $S_{\nu=2.3\text{GHz}}(\tau = 0.1)$ in mJy

^gWeighted least squares fit with errors in both variables to $Y = mX + b$ computed per Reed (1989)

^h $L_{\text{pre-flare}} - L_{5-10\text{hr}}$ in erg/s

ⁱ $L_{\text{pre-flare}} - L_{24\text{hr}}$ in erg/s

^jIncludes epoch 50590.16 for which some X-ray observations exist within a range spanned by the 10% uncertainty that was assigned to all flare start time estimates in Section 2.1

^kIndependent of the distance to source.

particular, we deduce the following results

1. The time averaged power required to launch the major flares, Q , is highly correlated with $L_{\text{pre-flare}}$ (Table 5).
2. $L_{\text{pre-flare}}$ is significantly elevated relative to the archival distribution of $L_{\text{intrinsic}}(1.2 - 50)$ for GRS 1915+105. (Figure 16, Section 4).
3. The time averaged power required to launch the major flares, Q , is correlated with L_{rise} (Table 5).
4. From Table 5, $Q + L_{\text{rise}}$ is highly correlated with $L_{\text{pre-flare}}$, with near equality if $D \approx 10.5$ kpc.
5. Columns (4) - (6) of Table 3 indicate that $L_{\text{intrinsic}}(1.2 - 50)$ increases in the hours that precede the stronger flares in the sample. There is a correlation between the amount of $L_{\text{intrinsic}}(1.2 - 50)$ increase (that extends to the decrease regime) and the strength of the subsequent flare (see Figure 19 and Section 5).

These findings are consistent with the interpretation that accretion rate is directly proportional to flare power, but elevated accretion in of itself does not guarantee that a major flare is ejected (in fact they usually are not).

Our data set spans nearly the full range of major flare power that covers a factor ~ 30 in estimated flare energy and a factor of ~ 5 in time averaged flare ejection power, Q . Based on the 2.3 GHz flux density, these flares approach energies and powers that rival the most powerful known flares since 1995.

Further radio and X-ray monitoring should be performed with high time resolution. This will allow the correlations described in this manuscript to be tested with more rigor and deeper physical connections should be revealed. From a physical point of view, the most critical to understand would be the connection between the variable X-ray luminosity during the launch phase and the identification of individual flux density peaks in high frequency VLBI images.

This article benefitted from a very knowledgeable referee who made many important improvements and suggestions. We would like to thank Vivek Dhawan for generously sharing his deep understanding of radio observations and his important data. We also are grateful for the useful comments on the manuscript generously pro-

vided by S. Markoff and S. Corbel. JR acknowledges partial funding from the European FP7 grant agreement number ITN 215212 “Black Hole Universe”, and the hospitality of ESO (Garching, Germany) where part of this work was done.

REFERENCES

- Belloni, T. et al 1997, ApJL **488** 109
 Belloni, T., Klein-Wolt, M., Mndez, M., van der Klis, M., van Paradijs, J. 2000, A & A **355** 271
 Blundell, K., Rawlings, S. 2000, AJ **119** 1111
 Corbel, S. et al 2000, A & A **359** 251
 Corbel, S., Nowak, M. A., Fender, R. P., Tzioumis, A. K., Markoff, S. 2003, A & A **400** 1007
 Dwahan, V., Mirabel, I.F., Rodriguez, L. 2000, ApJ **543** 373
 Dwahan, V., Muno, M., Remillard, R. 2004, in *X-Ray Timing 2003 Rossie and Beyond AIP Conference Proceedings*, Volume 714, pp.150-153 (2004)
 Done, C., Wardzinski, G., Gierlinski, M. 2004, MNRAS **349** 393
 Fender, R., Pooley, G., Brocksopp, C. Newall, S. 1997, MNRAS Letters **290** 65
 Fender, R. et al, 1999, MNRAS **304** 865
 Fender, R. et al, 1999, ApJL **519** 165
 Fender, R. and Pooley, 2000, MNRAS **318** L1
 Fender, R., Belloni, T., Gallo, E. 2004, MNRAS **355** 1105
 Fuchs, Y. et al, 2003, A and A **409** L35
 Gallo, E., Fender, R., Pooley, G. 2003, MNRAS **344** 60
 Ginzburg, V. and Syrovatskii, S. 1969, Annu. Rev. Astron. Astrophys. **7** 375
 Klein-Wolt, 2002, MNRAS **331** 745
 Lind, K., Blandford, R. 1985, ApJ **295** 358
 Marscher, A. and Gear, W. 1985, ApJ **298** 114
 Miller-Jones, J. et al 2005, MNRAS **363** 867
 Mirabel, I.F., Rodriguez, L., Cordier, B., Paul, J. and Lebrun, F. 1992, Nature **358** 215
 Mirabel, I.F., Rodriguez, L. 1994, Nature **371** 46
 Mirabel, I.F. et al 1998, A & A **330** L9
 Moffet, A. 1975 in *Stars and Stellar Systems, IX: Galaxies and the Universe*, eds. A. Sandage, M. Sandage & J. Kristan (Chicago University Press, Chicago), 211.
 Muno, M., Morgan, E, Remillard, R. 1999, ApJ **527** 321
 Pooley, G. and Fender, R. 1997, MNRAS **292** 925
 Prat, L., Rodriguez, J, and Pooley, G. 2010, ApJ **717** 1222.
 Punsly, B. 2005, ApJL **623** 9
 Punsly, B. 2012, ApJ **746** 91
 Rawlings, S., Saunders, R. 1991, Nature **349**, 138
 Reed, B. 1989, Am. J. Phys. **57** 642
 Reynolds, C. S., Fabian, A., Celloti, A., Rees, M. 1996, MNRAS **283** 873
 Reynolds, C., Punsly, B. Kharb, P., O’Dea, C. and Wrobel, J. 2009, **706** 851
 Rodriguez, J. Corbel, S., Kalemci, E., Tomsick, J. A., Tagger, M. 2004, ApJ **612** 1018
 Rodriguez, J. et al 2008, ApJ **675** 1436
 Rodriguez, J. et al 2008, ApJ **675** 1449
 Rodriguez, J., Varnière, P. 2011, ApJ **735** 79
 Rodriguez, L., Gerard, E., Mirabel, I.F., Gomez, Y., Velaquez, A. 1995, ApJSS **101** 173
 Rodriguez, L., Mirabel, I.F. 1999, ApJ **511** 398
 Rushton, A., Spencer, E., Fender, R. and Pooley, G. 2010, A & A **524** 29
 Sanders, R. H, 1983, ApJ **266** 73
 Trushkin, S. et al 2007 in *The Obscured Universe, Proceedings of the VI INTEGRAL Workshop July 2 - 8 2006*, Moscow, Russian Federation. Editor S. Grebenev, R. Sunayev, C. Winkler, ESA SP-622, Noordwijk, ESA Publication Division, ISBN 92-9291-933-2, p.357.
 Tucker, W. 1975, *Radiation Processes in Astrophysics* (MIT Press, Cambridge).
 Turler, M., Courvoisier, T., Paltani, S. 2000, A & A **361** 850
 Vadawale, S. et al 2003, ApJ **597** 1023
 van der Laan, H. 1966, Nature **211** 1131
 Willott, C., Rawlings, S., Blundell, K., Lacy, M. 1999, MNRAS **309** 1017